



Enhanced strength of additively manufactured Inconel 718 by means of a simplified heat treatment strategy

Jake T. Benzing^{a,*}, Nicholas Derimow^a, Orion L. Kafka^a, Nikolas Hrabec^a, Philipp Schumacher^b, Donald Godfrey^c, Chad Beamer^d, Priya Pathare^e, Jay D. Carroll^e, Ping Lu^e, Isaiah Trujillo^e, Frank W. DelRio^e

^a National Institute of Standards and Technology, Applied Chemicals and Materials Division, 325 Broadway, MS-647, Boulder, CO 80305, USA

^b SLM Solutions, Roggenhorster Str. 9c, 23556 Lübeck, Germany

^c SLM Solutions, 48561 Alpha Drive, Suite 300, Wixom, MI 48393, USA

^d Quintus Technologies, 8270 Green Meadows Dr. N, Lewis Center, OH 43035, USA

^e Sandia National Laboratories, Material, Physical, and Chemical Sciences Center, P.O. Box 5800, Albuquerque, NM 87185, USA

ARTICLE INFO

Associate Editor: Nima Shamsaei

Keywords:

Additive manufacturing

Hot isostatic pressing

Microstructure

Heterogeneities

IN718

Laser powder-bed fusion

ABSTRACT

This study simplified the heat treatment route and reduced the post-processing burden for laser powder bed fusion IN718 (a nickel-based superalloy). The tailored route retained advantageous microstructures and improved tensile strength when compared to the conventional post-processing strategy. The implementation of a single pre-aging step (combining the stress relief, HIP, and solution steps into one) and a single-step aging treatment (as opposed to two-step aging) resulted in a total heat treatment time of 15 h, which is far shorter than the conventional five-step strategy (42 h). The grain structure, pore structure, and room-temperature tensile properties were measured for three material conditions: the as-built condition, the baseline condition (a conventional five-step heat treatment route), and the HIP1020RQSA condition (novel high pressure rapid quenching HIP treatment followed by a single-step age). In the HIP1020RQSA condition, the high pressure (200 MPa), short hold time at a carefully selected temperature (0.5 h at 1020 °C), and rapid quenching (2150 °C/min) were implemented. Unique findings in the microstructure include generation of localized micro-scale recrystallization throughout the retained columnar grain and sub-grain structures, internal pore closure with a shortened HIP soak time, incomplete dissolution of Laves phase, and the absence of δ phase. The single step aging treatment also generated γ' and γ'' precipitates. The HIP1020RQSA treatment improved the yield strength of the baseline condition from 1112 MPa to 1209 MPa, decreased total elongation from 24.9% to 23.2%, and still exceeds the minimum Z direction (build direction) tensile properties outlined in ASTM F3055-14a.

1. Introduction

Advancements in manufacturing technologies, such as additive manufacturing (AM), have matured substantially in the last two decades (Kruth et al., 1998). In particular, metal alloys produced by laser powder-bed fusion (PBF-L), a layer-by-layer melting process, contain directional grain structures due to rapid solidification, directional cooling, and non-equilibrium phase transformations (Frazier, 2014). However, even in an optimized system, internal porosity and chemical heterogeneities are still observed in many AM parts due to melt pool variation within complex geometries, spatter, and stochastic variations in powder lots (Khairallah et al., 2016). Aside from these challenges, AM

of near net-shape parts has economic advantages over subtractive manufacturing methods, especially for nickel-based super alloys that are difficult to machine (Ezugwu et al., 1998). Nickel alloy 718 (IN718) is a prime example of this balance since the alloy is highly weldable (required for AM), has high work hardening rates (difficult to machine), and superior strength at room and elevated temperature when precipitation hardened (Lambarri et al., 2013). The latter properties, plus excellent corrosion resistance, propelled IN718 towards being a top choice in power generation, oil, gas, aerospace, nuclear, and marine applications (Akca and Gürsel, 2015).

The main driver behind the success of IN718, an austenitic (γ) nickel-based alloy enriched in Cr and Fe, is due to the numerous metallurgical

* Corresponding author.

E-mail address: jake.benzing@nist.gov (J.T. Benzing).

<https://doi.org/10.1016/j.jmatprotec.2023.118197>

Received 2 June 2023; Received in revised form 13 October 2023; Accepted 17 October 2023

Available online 21 October 2023

0924-0136/Published by Elsevier B.V.

processing-structure relationships that can be harnessed to distribute a range of phases throughout the microstructure (Table 1). A historical solidification diagram of IN718 that takes NbC into account was presented by (Knorovsky et al., 1989) beginning with the nucleation of primary dendritic γ . The liquid (L) enriches with Nb and C such that the formation of metal-carbon (MC) eutectic phase forms via $L \rightarrow \gamma + MC$ and depletes the liquid of Nb and C. As primary γ continues to solidify, the liquid re-enriches with Nb until solidification is terminated with the eutectic $L \rightarrow \gamma + \text{Laves reaction}$. The partitioning of MC (NbC in this case) from the liquid during primary γ growth results in dispersed MC phase in the interdendritic regions. The surrounding locations consist of the solute-rejected Nb-rich Laves phase that solidifies last. Previous studies have shown the precipitation of carbonitrides (Formenti et al., 2005) and Ti-nitrides (ANTONSSON and Fredriksson, 1992) can occur before the primary γ growth, acting as nucleation sites for NbC to precipitate from in the liquid. When cooling rates are very high ($> 10^3$ K/s) such as in PBF-L, cellular solidification of the γ phase is observed as opposed to dendritic solidification which contain secondary dendrite arms (Kou, 2003).

Previous studies have modeled the cellular/primary dendrite arm spacing as a function of cooling rate and temperature gradients in Ni-Nb alloys for AM applications using phase-field methods (Ghosh et al., 2017). Even more recently, a study coupled finite-element and phase-field methods to calculate the primary dendrite arm spacing (PDAS) to be in the range of 200–500 nm under PBF-L conditions (Karayagiz et al., 2020). In practice, the processing conditions in PBF-L paired with local heat gradients from re-melted layers above can cause a variety of PDAS across a single microstructure (Tao et al., 2019). Cellular colonies interspersed with interdendritic/solute-rejected Nb-rich Laves phase can resemble a classic grain structure when the colonies grow into each other. Due to subtle yet measurable changes in crystallographic misorientation at the dendritic cell walls present in as-built PBF-L material, these are classified as sub-grain boundaries (Kuo et al., 2018) and are formed across a wide range of processing conditions even when porosity is prevalent (Watringer et al., 2020). Due to the rapid solidification inherent to PBF-L processes, solute-trapping of Nb in the γ phase has also been observed, leading to Laves phase fractions of approximately 9% for a given interdendritic region (Tao et al., 2019). To accommodate the Laves-matrix incoherency along dendritic cell walls, a relatively high density of dislocation networks are typically observed and have also been linked to significant improvements in creep performance (Pröbstle et al., 2016). Additional carbide phases such as $M_{23}C_6$ and M_6C are possible in Ni-based superalloys, but the latter occurs due to high solubility of this phase with silicon in percentages over 0.4 wt% (Jena and Chaturvedi, 1984), which is now controlled for in PBF (ASTM F, 3055, 2021) processes. The Cr-stabilized Mo-rich $M_{23}C_6$ phase is still observed in case studies of IN718 through nucleation and growth on internal matrix features and grain boundaries, which is accelerated by strain within the microstructure (Aghajani et al., 2016).

Microstructures of IN718 in the as-built condition are typically undesirable for high-performance applications due to the presence of the Laves phase. Thus, IN718 builds are heat treated to dissolve the Laves phase back into the γ -matrix, which facilitates precipitation of the intermetallic strengthening phases (γ' and γ''). Depending on the heat treatment conditions, the γ' and γ'' phases can be independent, such that γ' precipitates are spheroidal whereas γ'' precipitates are disc shaped. Historical work by (Cozar and Pineau, 1973) demonstrated that γ'/γ'' can coprecipitate in the form of a γ' cuboid with a fully coherent γ'' shell across the six $\{100\}$ γ' faces. This shell inhibits Al, Ti, and Nb diffusion into γ' , therefore limiting coarsening and adding to thermal stability of the γ'/γ'' coprecipitates (He et al., 1998). The volume fraction of γ' is largely dictated by the (Ti + Al)/Nb ratio (Detor et al., 2018). Coprecipitation occurs when the γ' reaches a critical size and (Ti + Al)/Nb ratio between 0.9 and 1.0 (Cozar and Pineau, 1973), meaning that precipitation of γ' precedes that of γ'' . However, the γ'' phase became the most thermodynamically favorable phase when the ratio was 0.66

(Sundaraman et al., 1992). The γ'' is metastable and stoichiometrically equivalent to the incoherent orthorhombic δ phase. Thus, γ'' can lead to δ phase growth as needles/plates (at the expense of γ'') along the γ grain boundaries during longer heat treatments and reduces overall strength (Radavich, 2012). However, δ can be used to pin grain boundaries and control overall grain size (Mahadevan et al., 2010). In situ heat treatment and transmission electron microscopy (TEM) experiments have observed the precipitation of δ phase directly from a Nb-supersaturated γ matrix without the presence of γ'' , demonstrating that the solid state transformation of $\gamma'' \rightarrow \delta$ is not a prerequisite intermediary step (Dehmas et al., 2011).

It is with this overall understanding that selections are made when choosing post-processing parameters (e.g., heat treatment time, temperature, pressure, and cooling rate). Standard post-processing procedures for IN718 (AMS, 2774, 2020) typically require five independent steps for PBF-L IN718 parts: a stress relief, hot isostatic pressing (HIP), solution treatment, and two-step aging. The heat treatment time alone typically exceeds 40 h (assuming all steps conducted in one facility and accounting for cooling time) and will recrystallize the microstructure to achieve isotropic properties (Fayed et al., 2020). However, as-built PBF-L IN718 microstructures contain advantageous sub-grain structures that can be retained if grain boundary migration during post-processing is inhibited (Pröbstle et al., 2016). To achieve this, while still preparing the material for successful aging and high work hardening, a solution temperature chosen above the δ solvus should eliminate the brittle phases, dissolve the Laves phase for optimal solute segregation, and if the hold time is short enough, preserve some dislocations present near sub-grain boundaries (Gallmeyer et al., 2020). The δ solvus temperatures of PBF-L IN718 parts have been calculated to be within the range of 1010 °C (Gallmeyer et al., 2020) and 1040 °C (Jiang et al., 2019). In addition, a sufficiently fast cooling rate from solution to room temperature should be selected to avoid δ phase formation (Li et al., 2019). Given the advancement of HIP technologies to enable rapid quenching (Benzinger et al., 2019), it is possible to combine the HIP and solution steps as significant reductions in internal porosity begin at temperatures near the δ solvus (Tillmann et al., 2017), such that the isostatic pressure can plastically induce pore closure as material hardness progressively decreases with temperatures above 750 °C (Slama et al., 1997). Previous work (Varela et al., 2020) shows that a temperature of 1060 °C can induce recrystallization, indicating the HIP-solution temperature of interest falls within a narrow range (1010–1060 °C). Also, the stress relief temperature recommended for PBF-L IN718 falls within this temperature range. Finally, in terms of further improvements in productivity (Li et al., 2019) demonstrated that a single-step age (700 °C for 12 h) produced a modified γ' morphology throughout the microstructure.

The present study used a novel, lower HIP temperature to combine stress relief/HIP/solution into a single step that will prevent macro-scale recrystallization, retain advantageous sub-grain structures, prevent unwanted δ phase formation (high enough temperature and fast enough cooling rate), and generate enough dissolution of Laves phase in a single step. A subsequent single-step age, instead of the standard two-step age, was conducted to form γ' and γ'' precipitates. The microstructure and room temperature mechanical properties (hardness and tensile behavior) of this novel heat treatment are then compared to the as-built condition as well as a standard heat treatment that is nearly triple the total heat treatment time.

Table 1
Phases observed in Inconel 718.

Symbol	Crystal structure	Strukturbericht designation	Space group	Ordering	Stoichiometry	Constituents
γ	Face centered cubic	A1	Fm-3 m	Solid solution	-	(Ni,Cr,Fe)
γ'	Primitive cubic	L1 ₂	Pm-3 m	Intermetallic	A ₃ B	Ni ₃ (Al,Ti,Nb)
γ''	Body centered tetragonal	D0 ₂₂	I4/mmm	Intermetallic	A ₃ B	Ni ₃ (Ti,Nb)
δ	Orthorhombic	D0 _a	Pmmn	Intermetallic	A ₃ B	Ni ₃ (Ti,Nb)
Laves	Hexagonal	C14	P6 ₃ /mmc	Intermetallic	A ₂ B	(Cr,Fe,Ni) ₂ (Ti,Nb)
MC	Face centered cubic	B1	Fm-3 m	Carbide	AB	(Ti,Nb) (C,N)
M ₂₃ C ₆	Face centered cubic	D8 ₄	Fm-3 m	Carbide	A ₂₃ B ₆	(Ni,Co,Fe,Cr,Nb,Mo) ₂₃ C ₆

2. Materials and methods

2.1. Laser powder-bed fusion processing

The IN718 specimens were manufactured with an SLM 280 Production Series¹ dual laser powder-bed fusion machine and Argon gas atomized virgin, single-lot powder. Laser diffraction measurements of powder particles (ASTM, B822, 2020) yielded the following size range $D_V(10) = 18 \mu\text{m}$, $D_V(50) = 30 \mu\text{m}$, $D_V(90) = 50 \mu\text{m}$, where $D_V(X) = Y$ describes the diameter (Y) below which contains X volume fraction of material. Pre-build powder chemistry and post-build solid chemistry were measured (Table 2) to be within specification (ASTM F, 3055, 2021) for IN718. Solid chemistry measurements were conducted at an International Standards Organization (ISO) 17025:2017 compliant and Nadcap accredited test labs using Combustion-Infrared Absorption for Carbon and Sulfur (LECO CS600 and CS844), Thermal conductivity Nitrogen and Infrared Oxygen and Hydrogen Analyzer (LECO ONH836, for N, O, and H), and Inductively Coupled Plasma Atomic Emission Spectroscopy for the remaining elements. The parameters used for this build are summarized in Table 3. While contours were used to manufacture the parts, the microstructure and tensile properties were only measured in the hatch region, which is why contour parameters are not reported. The automated powder supply and permanent filtering modules were fitted to the SLM 280.

The entire build envelope (280 mm wide \times 280 mm long \times 365 mm tall) is organized into 25 regions and part IDs were embossed with a unique numerical label, shown in Fig. 1. Parts manufactured with a multi-laser overlap region (quadrants 11 through 15) were not used when evaluating tensile properties or grain structure. While additional witness coupons (squares in the X-Y plane of Fig. 1a) were manufactured to validate dimensional tolerances for a subsequent build, the current study only investigated rectangular parts (10 mm wide \times 54 mm long \times 25 mm tall). These parts were situated such that the width was roughly oriented with the gas flow direction (X), length relatively parallel to the recoater direction (Y), and height along Z, the build direction (Fig. 1).

2.2. Heat treatment parameters

Parts were removed from the build plates using electrical discharge machining, prior to any post-processing steps. Four rectangular parts were set aside for each material condition, (i.e., as-built, baseline, and HIP1020RQSA) so that one part could be analyzed for porosity, one part used for microstructure characterization, and two parts machined into tensile racks.

In all subsequent heat treatments, heating rates of approximately 12 °C/min were used, prior to a hold at a given temperature. The baseline material condition is based on a common heat treatment route

¹ Certain commercial software, equipment, instruments or materials are identified in this paper to adequately specify the experimental procedure. Such identification is not intended to imply recommendation or endorsement by the National Institute of Standards and Technology, nor is it intended to imply that the equipment or materials identified are necessarily the best available for the purpose.

used by various industries and follows standard procedures (AMS, 2774, 2020), detailed in Table 4. Under the hypothetical condition that the entire post-processing strategy could be completed in one facility and an oversimplification (linear assumption) of cooling rates, based on non-linear data extracted from literature on similarly sized parts (Baek et al., 2020), the linear schematic of temperature vs. time for the baseline post-processing strategy is shown in Fig. 2a, where SR indicates a stress relief, recommended HIP strategy, soln. indicates the solution heat treatment, followed by a two-step aging treatment. Also, logged data from the actual HIP cycle, which includes thermocouples placed in the top and bottom of the HIP chamber plus pressure readings, are shown in Fig. 2b for the baseline condition.

The HIP1020RQSA material condition involves heat treatment parameters that reduce the post-processing time from 42 h (baseline) to less than 15 h, which is visually depicted in Fig. 2c. The chosen temperatures were based on literature values of studies conducted in vacuum furnaces, but this work used a pressurized HIP chamber (200 MPa of argon) to conduct the solution step (Table 4). The hypothesis was that the chosen temperature will not introduce large-scale recrystallization (retain interdendritic boundaries/sub-grain boundaries), avoid δ formation by using a low temperature/short hold time/rapid quenching, and sufficiently reduce the total amount of internal porosity. During the rapid quench in the HIP chamber, an approximate cooling rate of 2150 °C/min was achieved between 1000 °C and 300 °C. Data logged during this HIP cycle is shown in Fig. 2d. The rapid cooling rate was achieved by using the Uniform Rapid Quench (URQ®) furnace making use of argon gas medium to accomplish the rapid cooling rates. The short single-step age was conducted in a vacuum furnace that was backfilled with a small amount of nitrogen.

2.3. Microstructural characterization

Parts from all material conditions were sectioned with a water-cooled high-speed saw to create 1.5 mm \times 2 mm \times 25 mm tall pieces. These specimens were analyzed with micro-X-ray Computed Tomography (X-ray CT) and an appropriate voxel edge length ($< 2 \mu\text{m}$) for detecting porosity. The X-ray CT measurements were conducted on a Zeiss Xradia Versa XRM-500 system and porosity was computed using a custom, open-source, Python-based image processing tool (Moser et al., 2023).

Additionally, parts from each condition were further sectioned along orthogonal planes (XY and XZ) and mounted in conductive bakelite media. The mounted samples were ground from 400 grit to 1200 grit using SiC paper, polished with a 1 μm diamond suspension, and vibratory polished for 24 h in a suspension of 50 nm colloidal silica. Electron backscatter diffraction (EBSD) measurements were performed at 200 fps and a step size of 0.5 μm in a field emission scanning electron microscope (FE-SEM) operated with a 20 kV accelerating voltage, 120 μm aperture, and a 19 mm working distance. Backscattered electron (BSE) images were captured from areas of interest to further assess the microstructure. Also, a focused ion beam (FIB) was used to extract transmission electron microscopy (TEM) lamellas for analysis with a scanning transmission electron microscope (STEM) operated at 200 kV and equipped with energy-dispersive X-ray spectroscopy (EDS) and a high-angle annular dark-field (HAADF) detector.

Table 2

Chemistry (% by mass) of ASTM F3055 requirements, the IN718 PBF-L virgin powder, and an as-built part (rough surfaces were removed).

Element	Ni	Cr	Fe	Nb[+Ta]	Mo	Ti	Al	Co	Si	C	O	N
ASTM F3055	50–55	17–21	Bal.	4.75–5.50	2.80–3.30	0.65–1.15	0.20–0.80	< 1.0	< 0.32	< 0.08	-	-
Powder	52.04	18.76	Bal.	5.01	3.07	1.00	0.53	0.10	0.04	0.03	0.02	0.01
As-built	52.59	18.84	18.14	5.35	3.22	1.10	0.57	0.08	0.055	0.03	0.018	0.008

Table 3

PBF-L machine parameters used for this PBF-L build.

Build parameter	Value
Scan order	Hatch-border
Build plate pre-heat temperature	200 °C
Layer height	30 µm
Laser spot size	75 µm
Rotation angle increment between layers	67°
Hatch distance	90 µm
Hatch laser power	200 W
Hatch scan speed	1200 mm/s

2.4. Tensile specimen machining and mechanical property measurement

Separate from the sectioned parts mentioned above, two additional rectangular IN718 parts from each material condition were machined into racks of 25 tensile specimens (Fig. 3) with gage dimensions of 4 mm (length parallel to build height) x 1 mm (width) x 1 mm (thickness). These racks were tested in an automated 2nd generation device described previously in (Heckman et al., 2020). Tensile specimens were pulled in displacement control at a rate of 0.05 mm/s (initial strain rate of $1.25 \times 10^{-2} \text{ s}^{-1}$) using a load frame equipped with an 8.9 kN load cell. The linear variable differential transformer (LVDT) used to move the frame of the high throughput setup was paired with the linear stage and controlled by a Temposonics R-series LVDT. Two cameras (Pointgrey 90 fps, 4.1 MPix) were used to capture images of samples during testing. The camera that captured images from the front of each tensile sample had a 0.5x lens attachment and a 1x adaptor. Also, three sets of light emitting diode lights with non-polarized white light provided illumination during digital image correlation (DIC) of the thickness dimension of each tensile sample (white paint as a background, black speckle pattern with a 12-pixel width and a 6-pixel gap between speckles). The camera that computed strain from images on the side of each tensile sample had no lens attachment with a 12 zoom lens and a 2x adaptor. Using VicGauge2D, strain was computed by a virtual extensometer along the gage length using two subsets (approximately 90 pixels x 90 pixels). The approximate field of view calibration of 1.9 µm/pixel was used to compute engineering strain. In addition to extracting engineering stress-strain properties, work hardening rate was evaluated for representative samples. For all strain values less than the strain

corresponding to the ultimate tensile strength (uniform elongation), the raw data was smoothed by 2 passes of a MATLAB-based moving average filter with a window size of 15 data points so that a derivative could be calculated. The derivative of true stress and true strain was then calculated using a moving window of approximately 45 data points.

As a measure of another mechanical property, nine macro-scale hardness measurements were performed on the XY plane of polished samples for each material condition using a certified indenter system (Rockwell hardness, ASTM E18 compliant, C scale, diamond tip, 150 kg). An analysis of variance (ANOVA) was completed with InStat software (Tukey test) and used to test the null hypotheses that the tensile properties and hardness values were equal across material conditions; significance is defined as $p < 0.01$.

3. Results

3.1. Grain characteristics, sub-grain structures, and nano-scale precipitates

Beginning with fields of view that are 1 mm x 1 mm in area, the grain orientations revealed in inverse pole figure (IPF) maps were measured across XY and XZ planes. Also, an intensity map of poles oriented with

Table 4

Post-processing parameters, where AC = air cool, FC = furnace cool, and RQ = rapid quench. Hot isostatic pressing was performed at Quintus Technologies Application Center in a modern QIH 15 L HIP unit.

Material condition	Stress relief	Hot isostatic pressing	Solution	Aging
As-built	-	-	-	-
Baseline	1065 °C, 20 Pa of nitrogen, 1.5 h, AC	100 MPa of argon, 1150 °C, 4 h, FC	1066 °C, 20 Pa of nitrogen, 1 h, RQ	718 °C, 20 Pa of nitrogen, 8 h, FC to 621 °C, 10 h at 621 °C, FC
HIP1020RQSA	-	200 MPa of argon, 1020 °C, 0.5 h, RQ	-	700 °C, 20 Pa of nitrogen, 12 h, RQ

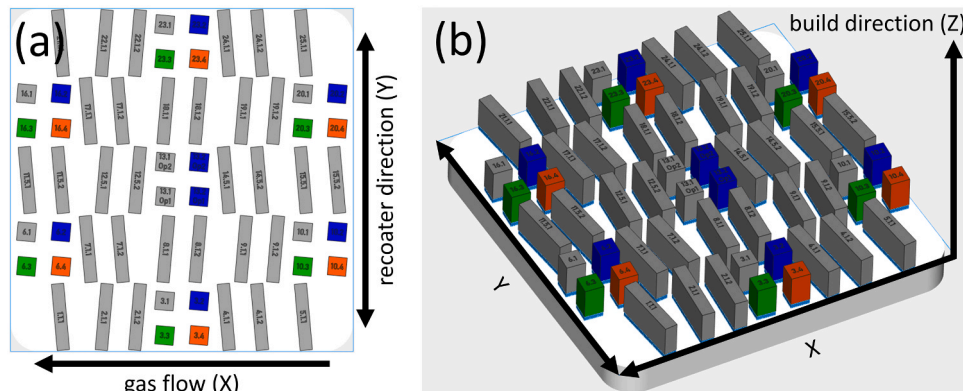


Fig. 1. Build layout of PBF-L IN718 parts: (a) top view and (b) isometric view, where X = gas flow direction, Y = recoater direction, and Z = build direction.

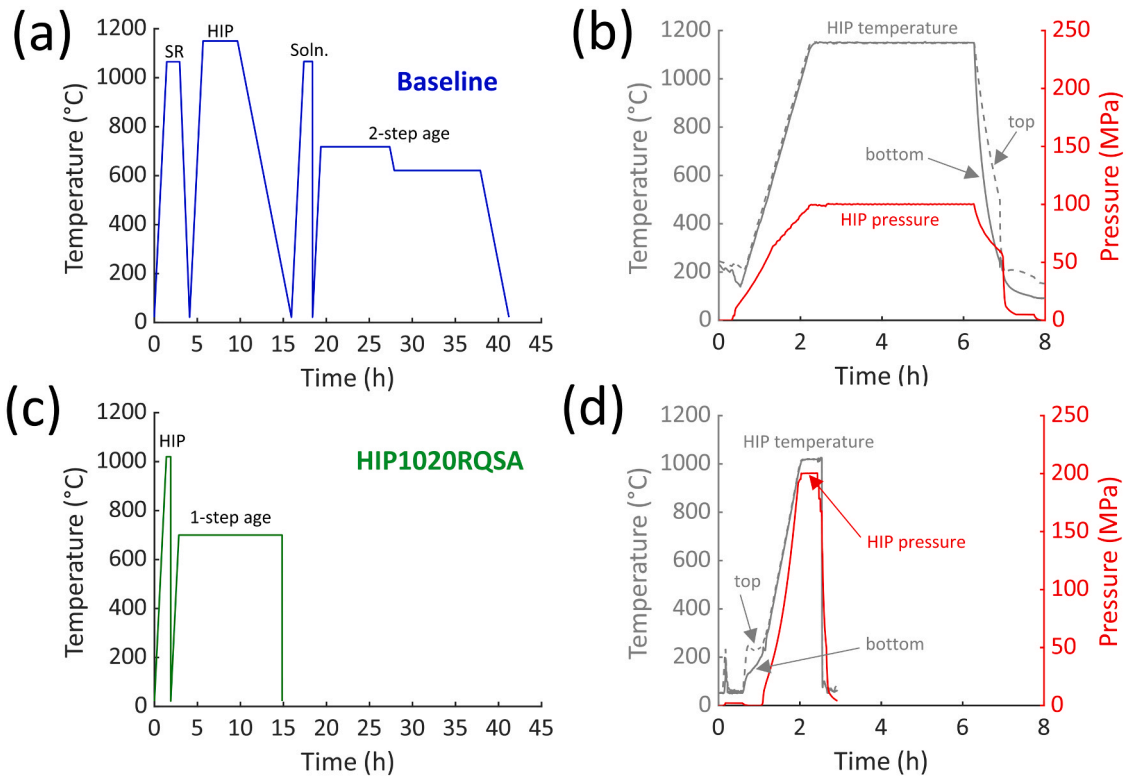


Fig. 2. (a/c) Linear schematic and overview of entire post-processing strategy for the (a) baseline and (c) HIP1020RQSA conditions. Actual time-temperature-pressure data recorded during HIP treatments are shown for the (b) baseline and (d) HIP1020RQSA conditions and arrows indicate temperatures values recorded by separate thermocouples at the top and bottom inside the HIP vessel.

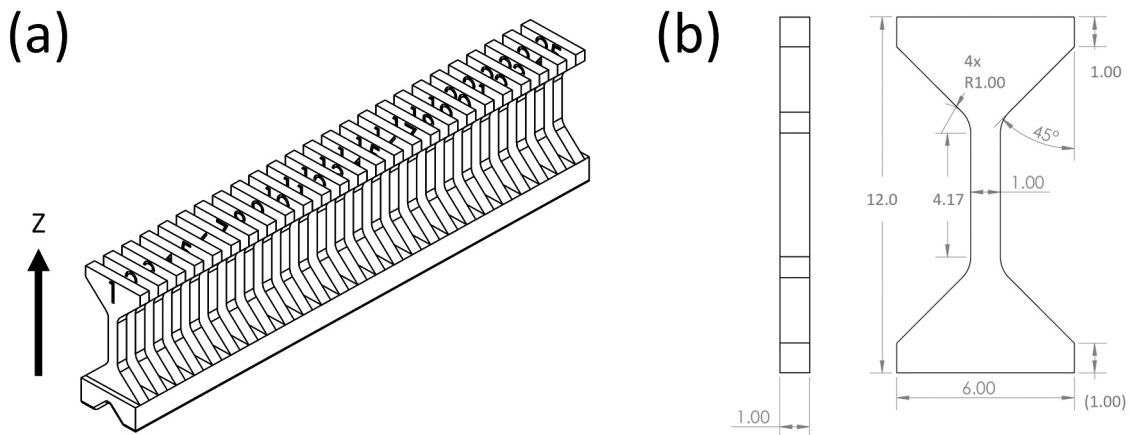


Fig. 3. Drawings used to machine PBF-L IN718 parts into (a) tensile rack with (b) with gage dimensions of 4.17 mm long x 1 mm wide x 1 mm thick. All drawing dimensions in mm.

respect to Z was plotted. These are shown for the as-built condition (Fig. 4a-c), the baseline condition (Fig. 4d-f), and the HIP1020RQSA condition (Fig. 4g-i). In the XY plane of the as-built condition, laser melted scan tracks are visible in the grain structure (diagonally oriented in Fig. 4a), whereas teardrop shaped melt pools are oriented vertically in the XZ plane (Fig. 4b). Harmonic series expansions with no sample symmetry assumed are used to compute the spread of integrated intensities in the IPF heat map shown in Fig. 4c, which indicates the {100} poles are oriented parallel to the build direction (Z) and these poles constitute most of the integrated intensities. In stark contrast, the baseline condition's microstructure contains equiaxed grains and annealing twins in both the XY and XZ planes (Fig. 4d-e), plus no preferred orientations with respect to the build direction (Fig. 4f). The

HIP1020RQSA condition's microstructure resembles the as-built microstructure (melt tracks still visible in the XY plane and melt pools in the XZ plane) as shown in Fig. 4g-h. However, the overall {100} texture in the as-built condition has weakened in intensity and shifted slightly in character for the HIP1020RQSA condition to a mix of {100} and {101} poles that are parallel to the build direction (Fig. 4i).

While not visible at the magnifications depicted in Fig. 4, porosity was detected with SEM. However, pore metrics were quantified with X-Ray CT. While the as-built condition did contain some pores with the largest single dimension exceeding 40 μm, the total porosity by volume was low (0.0140%). The HIP parameters selected for the baseline and HIP1020RQSA conditions were effective in reducing porosity (Table 5) by at least an order of magnitude in volume percent. The largest pore

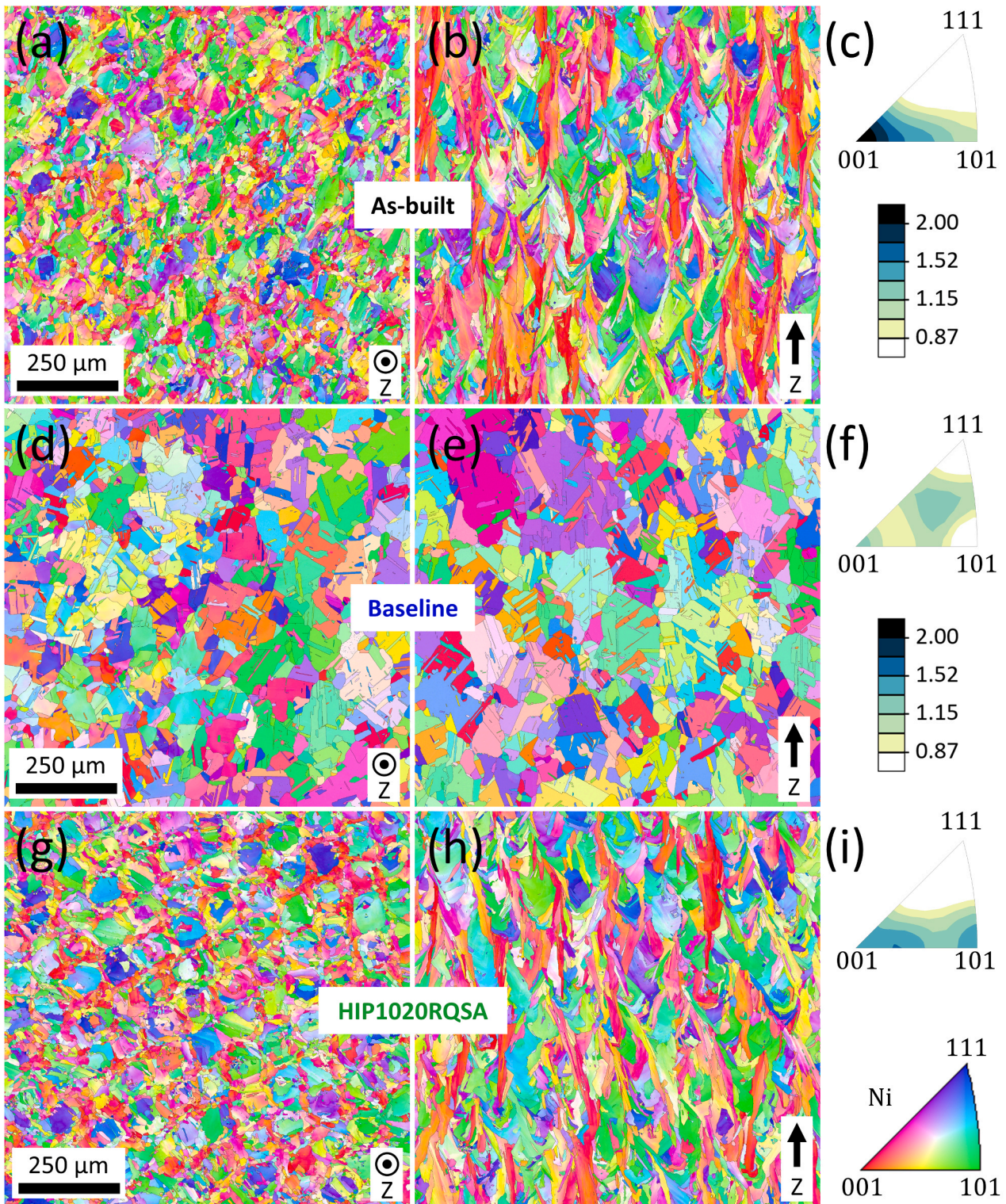


Fig. 4. Inverse pole figure maps of the (a-c) as-built, (d-f) baseline, and (g-i) HIP1020RQSA material conditions recorded on (a,d,g) XY planes and (b,e,h) XZ planes. The (c,f,i) integrated intensities of poles parallel to Z are plotted using the same maximum value in multiples of uniform random distribution (m.r.d.). The inverse pole figure color legend applies to all maps and the coordinates (001, 101, and 111) apply to the integrated pole figures. At this magnification, the as-built and HIP1020RQSA grain structures resemble one another, including grain elongated along Z, but the as-built condition has a higher degree of texture. The baseline condition contains equiaxed grains and no texture, indicating recrystallization.

observed after HIP was approximately 4 μm in diameter and spherical in nature.

In terms of other quantitative metrics, the average area of each grain in the as-built, baseline, and HIP1020RQSA microstructures are 841 μm², 2896 μm², and 842 μm² in the XY plane and 3013 μm²,

3781 μm², 2699 μm² in the XZ plane. In terms of a grain diameter equivalent for the baseline condition where equiaxed grains are observed, these grain size areas translate to diameters of 61 μm (XY plane) and 69 μm (XZ plane). An additional metric of interest was grain shape orientation (Fig. 5), where a major axis orientation value of 90°

Table 5
Total porosity measured with X-ray CT.

Material condition	Porosity (% volume)
As-built	0.0140
Baseline	0.0002
HIP1020RQSA	0.0006

means a given grain's longest axis is aligned with the vertical axis of the maps shown in Fig. 4. Given the equiaxed nature of grains in the baseline condition, which indicates complete recrystallization, the grain shape distributions (Fig. 5c-d) appear relatively flat across axis orientations from 0° to 180°, with the exception of small peaks observed between 60° and 100° in the XZ plane. When compared to the XZ plane shape orientation of the as-built condition however, these small peaks in the

XZ plane distribution of the baseline condition are likely related to a preferential growth direction inherited from the columnar grains found in the as-built grains structure (Fig. 5b). Within the XY plane of the as-built and HIP1020RQSA condition (Fig. 5a and Fig. 5e), grain shape orientation is highly dependent on Z height as the PBF-L scan strategy rotates on every XY plane. While the general distribution shape of the grain shape orientation in the XZ plane of the HIP1020RQSA condition (Fig. 5f) does generally match the as-built condition (Fig. 5b), the average major axis orientation shifted lower and has a wider spread (Table 6).

Partial recrystallization was thought to have possibly occurred to explain the changes in the major axis orientation observed in the XZ plane. Thus, grain reference orientation deviation (GROD) angle maps were generated near suspected areas of minor recrystallization in the HIP1020RQSA condition and directly compared to equivalently sized

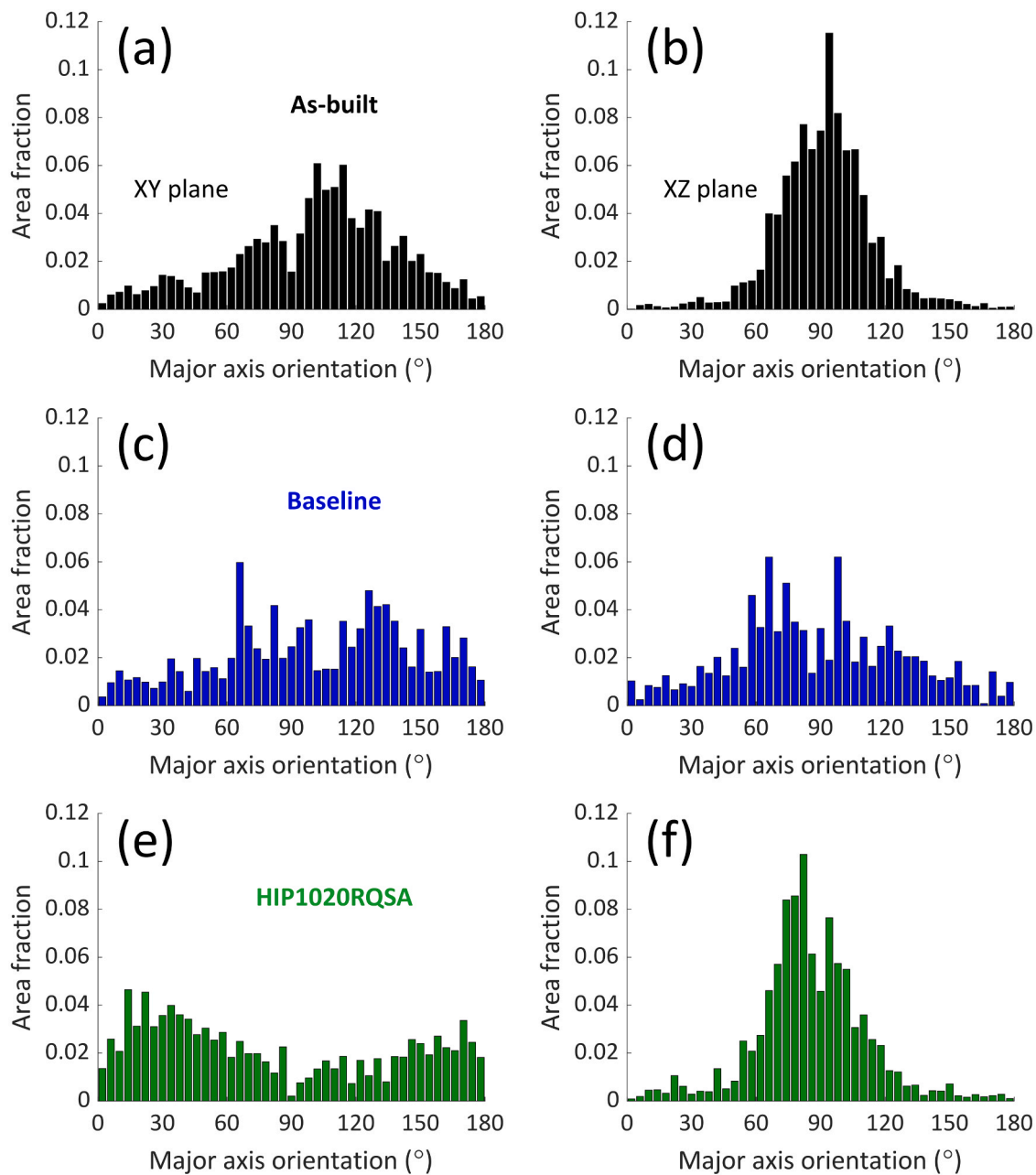


Fig. 5. Grain shape orientation analysis of EBSD data provided for the (a-b) as-built, (c-d) baseline, and (e-f) HIP1020RQSA material conditions and recorded on (a,c, e) XY planes and (b,d,f) XZ planes. The grains in the baseline condition don't exhibit an oriented distribution along the Z direction in the XZ plane (90° of major axis orientation is parallel to Z), but the as-built and HIP1020RQSA grains do show Z dependence with respect to grain shape.

Table 6

Average grain shape orientation (90 is equal to being parallel with the vertical axis of each map) measured with EBSD. Ranges indicate 1σ standard deviations.

Material condition	Major axis orientation in XY plane ($^{\circ}$)	Major axis orientation in XZ plane ($^{\circ}$)
As-built	100 ± 38	92 ± 22
Baseline	101 ± 44	89 ± 39
HIP1020RQ+SA	81 ± 55	85 ± 26

fields of view in the other conditions (Fig. 6). The GROD maps offer a quantitative crystallographic description on the amount of intragranular misorientation found within a given grain, where each grain's average orientation is set as the reference angle. In the as-built condition (Fig. 6a), a large spread in intragranular misorientation (orientation angle gradients) is seen from a couple degrees up to 10° and sub-granular boundaries are visible as diagonally oriented steps within a given grain (found mostly in larger columnar grains). The GROD map of the baseline condition (Fig. 6b) indicates little to no misorientation within any grain, which is a strong indicator of recrystallization. The grain structures of the HIP1020RQSA condition visible in the GROD map (Fig. 6c) show similarities to both the as-built condition and baseline condition in that large columnar grains with substantial orientation gradients are present. However, there is also a $32\ \mu\text{m}$ wide cluster of small equiaxed grains (from $2\ \mu\text{m}$ to $9\ \mu\text{m}$ in diameter) with little to no intragranular misorientation (less than 3°), indicating localized areas of recrystallization exist and could account for a shift in major axis orientation distribution extracted from a much larger area.

Upon higher magnification inspection of the microstructure using BSE imaging techniques in the FE-SEM (BSE contrast is sensitive to electron channeling and atomic number of a given phase), sub-granular structures comprised of dislocation networks and Laves are visible in the XY plane of the as-built condition (Fig. 7a, white circles within grains). In the baseline condition, planar annealing twins and small dark carbides are visible within a given grain, plus bright Nb-rich particles are situated on grain boundaries and within grains (Fig. 7b). Most interestingly is the grain/sub-grain structure of the HIP1020RQSA condition where subtle changes in BSE contrast are observed at a size scale that is reminiscent of the sub-grain structure observed in the as-built condition, but without the dislocation networks/entanglements. These changes in contrast correspond to circular features that are approximately $1\ \mu\text{m}$ in diameter or less (Fig. 7c). If these features are indeed recrystallized grains or sub-grain boundaries with low-angle misorientation, it is possible that these features are not indexed in the XY plane as new grains by EBSD (Fig. 4g) due to step size ($0.5\ \mu\text{m}$) or the defined grain tolerance angle (5°). To determine if these sub-grains were truly equiaxed, the XZ planes of the as-built and HIP1020RQSA conditions were compared using BSE imaging in a FE-SEM, plus bright-field (BF) and HAADF imaging of FIB lamellae in a STEM, shown in Fig. 8. The as-built condition contains columnar sub-grain boundaries decorated with Nb-rich precipitates entangled with a high density of dislocation networks along the interdendritic boundary formed during rapid solidification (Fig. 8a). The dislocation defect structures are wavy in nature (Fig. 8b-c), found mostly within sub-grains (between dendrite arms), and in some cases clustered around dark spherical nano-scale carbides (Fig. 8a-b). Similarly, the HIP1020RQSA sub-grain structure is columnar, disproving the idea of an equiaxed sub-grain structure. However, differences in sub-grain structure are noticeable in that the Nb-rich precipitates are not as visible, even at high magnification, plus the dislocation networks within sub-grains are virtually non-existent (Fig. 8d-f) when compared to the extreme case of the as-built condition. Dark spherical carbides are still present in the HIP1020RQSA condition (Fig. 8d-e).

Continued inspection of which micro-scale and nano-scale phases are present in all the material conditions required STEM-EDS measurements at appropriate length scales. STEM-EDS analysis of the sub-grain boundaries in the as-built condition revealed Nb-rich irregularly

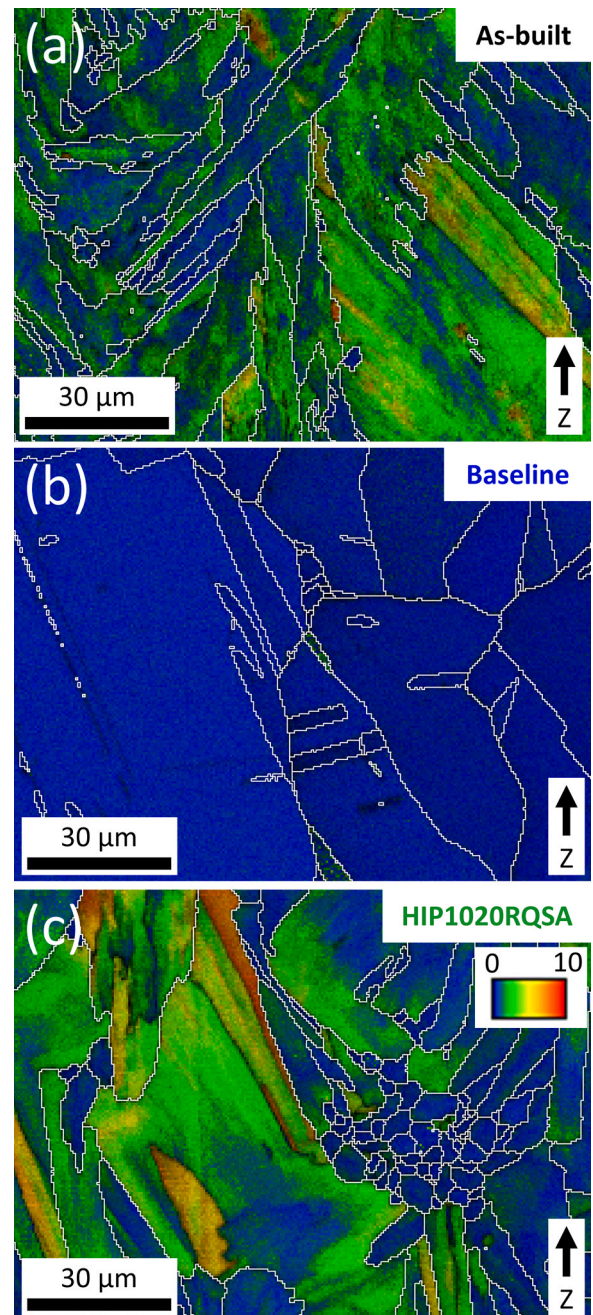


Fig. 6. Grain reference orientation deviation angle maps of areas of interest along XZ planes in the (a) as-built, (b) baseline, and (c) HIP1020RQSA conditions. The color legend in (c) applies to all maps. The as-built condition contains grains with high degrees of intragranular misorientation. Grains in the baseline condition have a low intragranular misorientation and annealing twins are observed. Grains in the HIP1020RQSA condition contain a mix of high and low misorientation with the latter focused in a small region containing micro-scale equiaxed grains.

shaped Laves phase heterogeneously distributed within a grain (non-continuous in a given XZ or XY plane), plus Nb- and Ti- carbides among and between the bright Laves phases (Fig. 9a). In addition, Ti- and Al-oxides were occasionally observed. At the same magnification, the HIP1020RQSA condition revealed comparatively very thin strips of a Nb-rich phase (not present on every sub-grain boundary), plus similarly sized carbides and oxides (Fig. 9b). Higher magnification (Fig. 9c) was required to inspect the Nb-rich strips more accurately. The atomic percentages of Ni and Nb were compared for the Nb-rich regions shown in

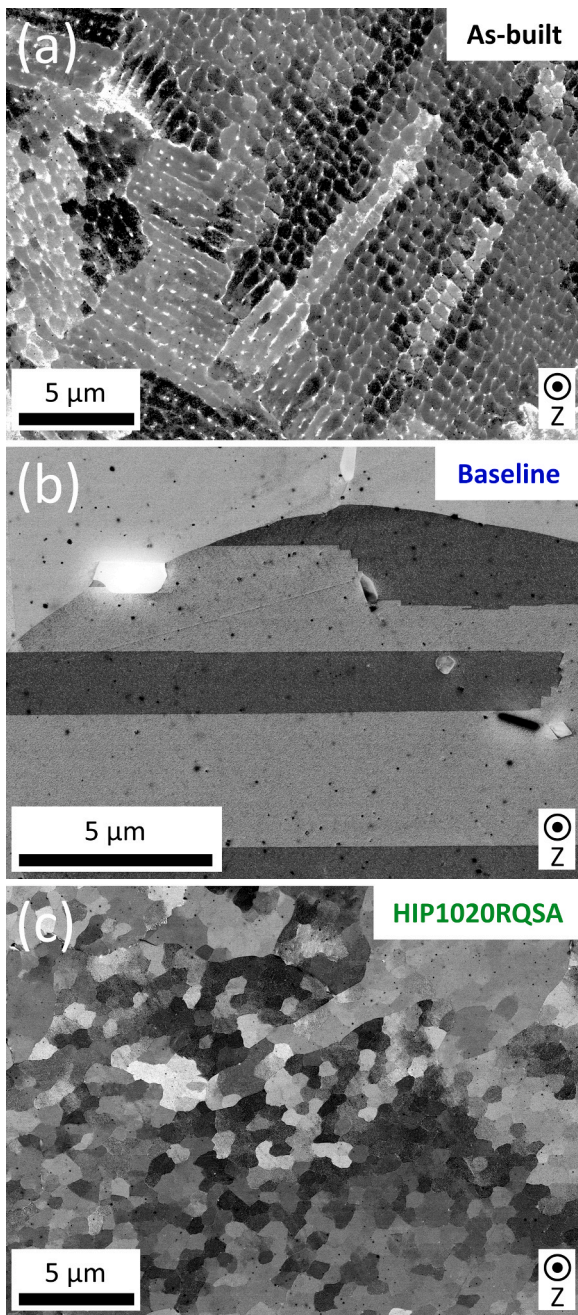


Fig. 7. BSE images recorded on the XY plane of the (a) as-built, (b) baseline, and (c) HIP1020RQSA material conditions highlighting the (a) as-built sub-grain structure, (b) precipitates and carbides distributed throughout grains in the baseline condition, and (c) a modified sub-grain structure in the HIP1020RQSA condition.

Fig. 9. Normalizing the atomic ratios of Ni to Nb for these regions revealed that the relative percentage of Nb to Ni in the HIP1020RQSA condition is consistent with that of the interdendritic as-built region. This therefore indicates that the Laves phase in HIP1020RQSA condition is still present, albeit in a significantly smaller phase fraction due to incomplete dissolution of this phase during the HIP1020RQSA treatment. Also, since the baseline and HIP1020RQSA conditions were respectively subjected to two-step and single-step aging treatments, additional STEM-based measured were incorporated to confirm the presence of nano-scale strengthening precipitates. In Fig. 10a, the region indicated in the HAADF image shows a region of contrast approximately 35 nm wide and after confirmation with fast Fourier transformation

(FFT) analysis of super lattice reflections extracted from an image acquired at atomic resolution, the presence of γ' precipitates was confirmed. As FFT alone cannot distinguish between γ' and γ in the zone axis of the atomic resolution HAADF image, STEM-EDS was also employed. To confirm if the precipitates are distributed throughout the matrix, both high and lower magnification STEM-EDS maps were recorded. The locations of the Al-containing γ' phase is respectively highlighted with Al counts maps, the γ' phase by Nb counts maps, and the γ matrix by Cr counts maps as the precipitates stoichiometrically do not favor inclusion of Cr.

3.2. Mechanical properties and fractography

The quasi-static tensile behavior of each material condition was evaluated at room temperature using an automated high throughput setup. The tensile direction is parallel to the build direction. Two racks of 25 tensile specimens were tested for each of the three unique material conditions, totaling 150 specimens. Each individual rack is assigned an ID that is slightly shorter than material condition designations previously described for brevity. As an example, the tensile rack excised from part number 1.1.1 and the as-built condition is deemed As-1 (Fig. 11a). The engineering stress-strain responses from all tests, including the unloading and reloading portion of the test used to measure modulus, is shown in Fig. 11. It is generally apparent that the as-built condition had the greatest ductility (Fig. 11a-b), whereas the baseline (Fig. 11c-d) and HIP1020RQSA (Fig. 11e-f) conditions possessed less ductility, but greater tensile strengths. The latter trend in strength is also consistent with macroscopic hardness measurements provided in Table 7.

To enable a direct comparison across all conditions and stress-strain responses, the medians, 25th and 75th percentiles, minimum, maximum, and outliers of the engineering tensile properties are plotted in Fig. 12. In terms of yield strength (YS), the relative total range (minimum to maximum, i.e., lower whisker to upper whisker) for a given data set is relatively similar, except for HRQ-1, which shows a tight spread and approximately half the range as other data sets. The largest range in YS is 89 MPa (Base-1 in Fig. 12a) and the largest range in ultimate tensile strength (UTS) is 93 MPa (Base-2 in Fig. 12b). The data set exhibiting the lowest median YS of 699 MPa is from the as-built condition (As-1) and the greatest median UTS of 1403 MPa is found in the HIP1020RQSA condition (HRQ-2). Moving towards comparisons of ductility, the strain value at UTS is defined as the amount of uniform elongation (UE), whereas the total elongation (TE) is measured after failure in the gage section for a given tensile test. All data sets show a relatively similar range for UE and TE, except for the HRQ-2 data set, which has a range that is approximately one third of the largest TE range (not including outliers). The lowest median UE of 14% is from the HIP1020RQSA condition (HRQ-2 Fig. 12c) and the greatest median TE of 36% is from the As-built condition (As-2 in Fig. 12d).

Further, all engineering tensile properties were subjected to ANOVA, and it was found that the differences between tensile racks originating from the same material condition (e.g. As-1 and As-2) were not significant ($p > 0.05$). Therefore, the two data sets in each material condition were combined into one data set (50 tensile curves per material condition, not including outliers) and treated again with ANOVA. The differences between the three material conditions were deemed extremely significant ($p < 0.001$). The average and standard deviation of all engineering tensile properties for each material condition is provided in Table 8. It is apparent that the aging treatments had a positive effect on the average elastic modulus measured during unloading as the as-built modulus increased from 141 GPa to 171 GPa (Baseline) and 162 GPa (HIP1020RQSA). The average yield strength of the HIP1020RQSA condition (1209 MPa) was nearly 100 MPa greater than the baseline condition (1112 MPa). Also, the as-built UE (24.5%) and TE (34.8%) indicates a superior strain hardening capacity as compared to the baseline (16.8% UE, 24.9% TE) and HIP1020RQSA (15.2% UE, 23.2% TE) material conditions. This was further examined with representative

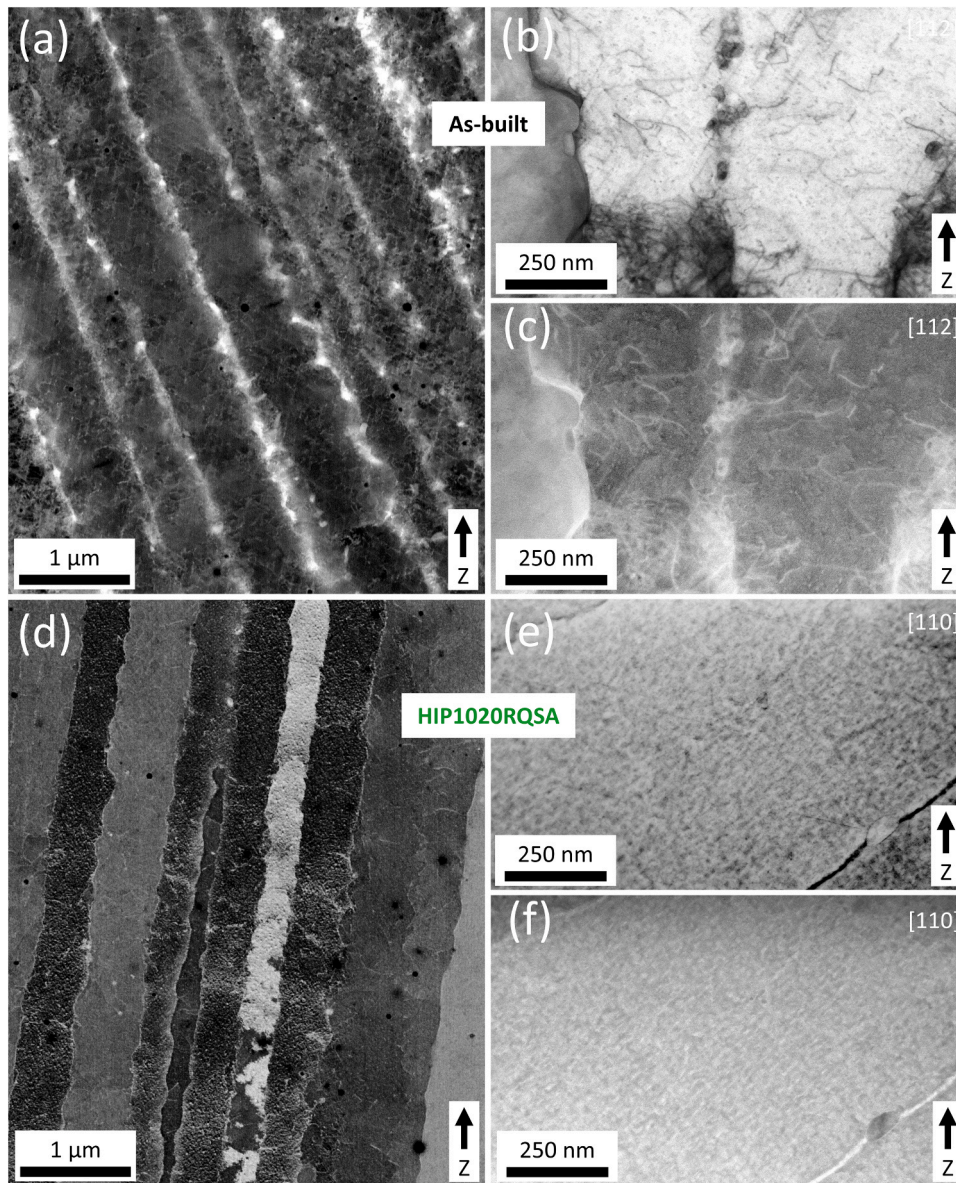


Fig. 8. (a,d) BSE images recorded with SEM, (b,e) BF images recorded with STEM, and paired (c,f) HAADF images all taken such that the build direction is roughly parallel with the vertical direction for the (a-c) as-built and (d-f) HIP1020RQSA material conditions. Most notably, a reduction in dislocation content and Laves phase along sub-grain boundaries is noted in the HIP1020RQSA condition.

tensile specimen data sets in Fig. 13a through conversion of engineering to true stress-strain behavior and derivation of the work hardening rate. While the baseline and HIP1020RQSA work hardening rates are nearly identical, the as-built work hardening rate is consistently greater from 0.05 true strain all the way to the onset of necking (UTS). This high work hardening capacity will be examined and compared later in terms of grain structure since fractography consistently revealed expanded porosity and cracks between porosity (Fig. 13b), whereas features that potentially resemble unsealed porosity in the baseline (Fig. 13c) and HIP1020RQSA (Fig. 13d) fracture surfaces were substantially smaller than seen on as-built fracture surfaces. All material conditions did contain microvoid coalescence on all investigated fracture surfaces.

4. Discussion

Improvements in the understanding of processing-structure-property (PSP) relationships have occurred as more industries are adopting AM, but standard post-processing routines are not well optimized for

microstructures found in additively manufactured parts (Krueger, 2017). The microstructures of metal parts produced by AM naturally experience rapid solidification and metastable phase transformations, which can create opportunities for microstructure manipulation to unlock unique properties. The latter is especially true in solid solution strengthened face-centered cubic alloys, where PBF-L processes result in highly tangled dislocation cell structures (Zhu et al., 2018). In steels, the cell size has been controlled through changes in laser scanning speed, and in-situ TEM imaging during externally applied loading (Liu et al., 2018) demonstrates how the entangled cell walls trap partial dislocations generated during plastic deformation, enabling a Hall-Petch effect. While this effect can be quantified with grain size and sub-grain (dislocation cell) size metrics (Mecking and Kocks, 1981), the additional strain hardening contributions from aging of nano-scale precipitates in Ni-based super alloys creates more opportunities for exploring PSP relationships (Pröbstle et al., 2016). The current work builds on the previous studies involving solution temperature optimization for PBF-L IN718 (Gallmeyer et al., 2020), aging time reduction

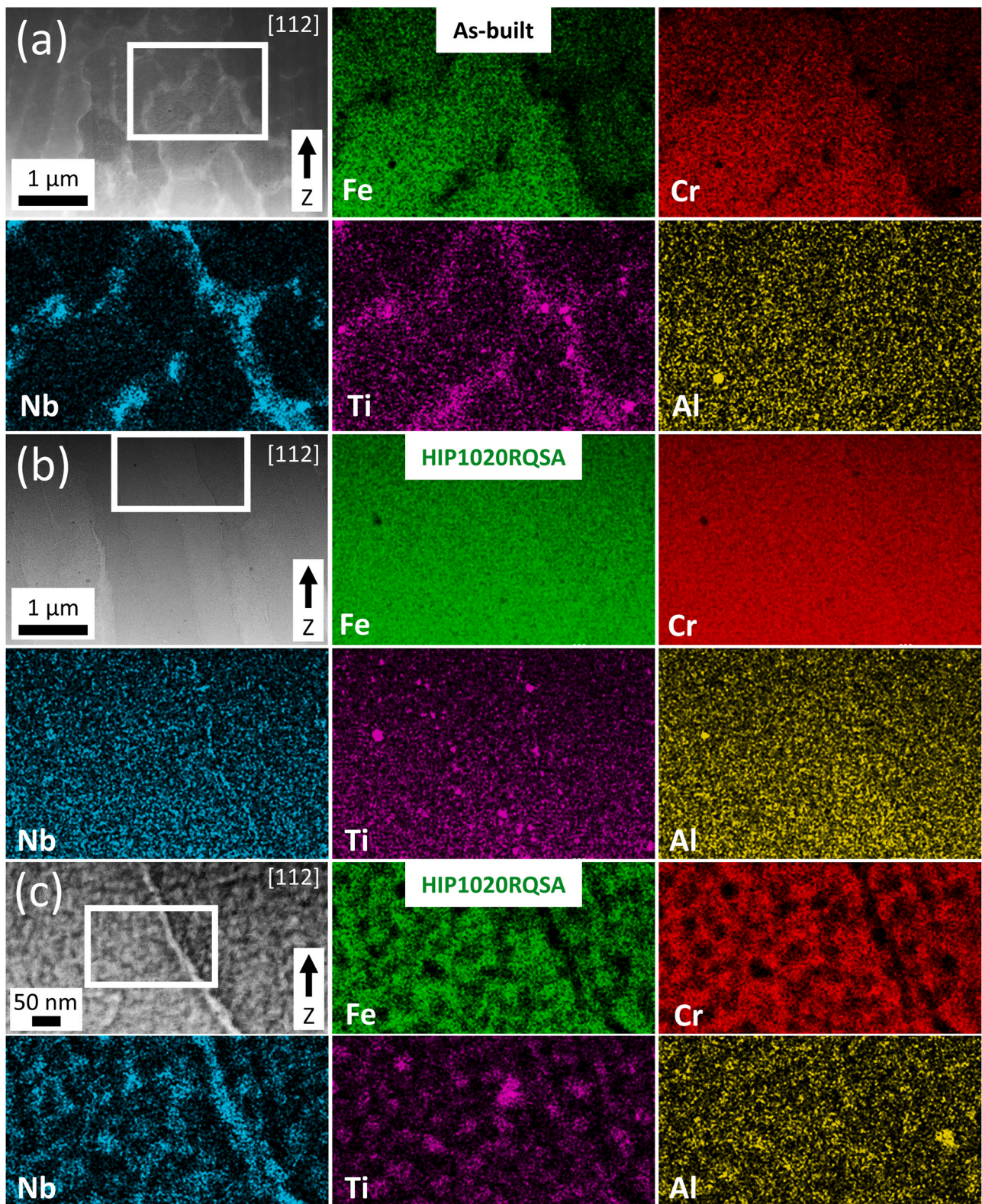


Fig. 9. Sub-grain boundaries parallel to the build direction of (a) as-built and (b,c) HIP1020RQSA material conditions were analyzed with STEM-based techniques such that a (a-c) HAADF image was acquired and a subset of that area (indicated by a white rectangle) was analyzed with EDS. Counts-based maps of Fe, Cr, Nb, Ti, and Al are provided for identification of the main metallic elements that indicate the presence of Laves phase, carbides and oxides. Zone axis alignment is indicated in the HAADF images.

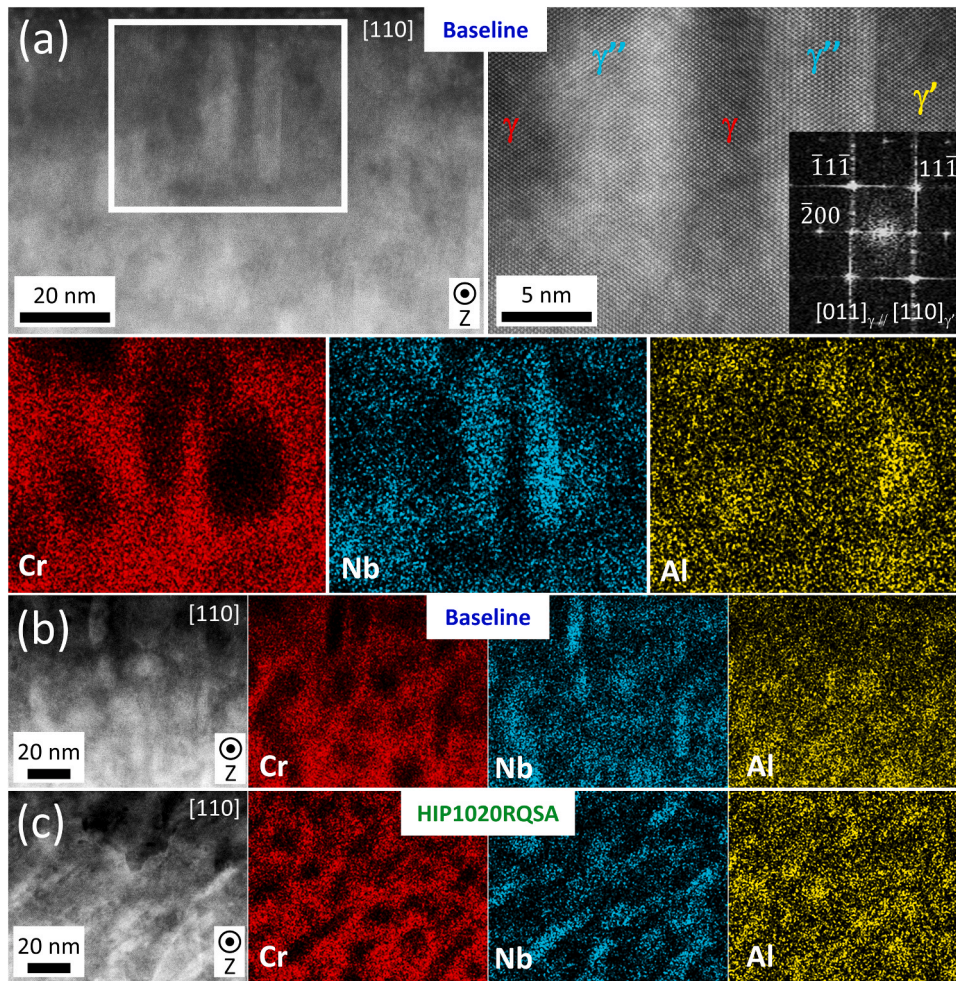


Fig. 10. Strengthening precipitates observed after aging for the (a,b) baseline and (c) HIP1020RQSA material conditions were analyzed with STEM-based techniques such that a (a-c) [110] zone axis was aligned, a HAADF image was acquired and a subset of that area (indicated by a white rectangle) was analyzed with EDS. The secondary HAADF image in (a) recorded with atomic resolution was analyzed with FFT (see inset). Counts-based maps of Cr, Nb, and Al are provided for respective identification of γ' and γ'' phases present as nano-scale structures within the γ matrix.

approaches for PBF-L IN718 (Li et al., 2019), and experimental hot isostatic pressing strategies for PBF-L IN718 (Varela et al., 2020). The unique findings in the current work and additional contributions to the literature with the HIP1020RQSA condition include identification of small regions with recrystallized grains, significant reduction in porosity using only 0.5 h of HIP soak time, observation of remaining Laves phase along the retained sub-grain boundaries, and statistics-based confirmation of improved strength in 0° oriented (tension parallel to build direction) specimens after 12 h of aging time (excluding cooling time).

Similar grain characteristics shared between the as-built and HIP1020RQSA condition were presented such as crystallographic texture, grain structure shape, and intragranular misorientation. However, slight differences were revealed through quantitative analysis of EBSD data (Fig. 4). The $\{100\} \parallel Z$ texture character in the as-built condition had a max intensity of 2.3 multiples of uniform random distribution (m.r.d.) and after treatment, the HIP1020RQSA condition exhibited a mixed $\{100\}$ and $\{101\} \parallel Z$ character with a max intensity of 1.5 times random. While a reduction in intensity is typically expected after solution treatments in the γ phase field due to slight decreases in misorientation, a change in character is indicative of some type of recrystallization (Zhao et al., 2020). From a macroscopic view, the grain structure of the HIP1020RQSA condition closely resembled the as-built microstructure (teardrop shaped melt pools oriented vertically in the XZ plane). Direct observation of small regions containing equiaxed grains in the HIP1020RQSA condition were observed, which contained low

amounts (less than 3°) of intragranular misorientation (Fig. 6). The latter is an accepted indicator of recrystallization (Haase et al., 2015). Although the mechanism of recrystallization was not isolated in this study, previous work on HIP of AM metals has shown that even when the macroscopic grain structure does not fully recrystallize, pore closure from isostatic pressure at high temperatures has been linked to the creation of small regions with equiaxed grains (Benzing et al., 2019). Also, if a pore is situated within a grain, the nearby high intragranular misorientation present in as-built IN718 grains could provide an opportunity for dynamic recrystallization (Zhang et al., 2021). From a size scale perspective, the largest pore in the as-built condition was approximately $40 \mu\text{m}$ and the region containing small equiaxed grains in the HIP1020RQSA condition was approximately $32 \mu\text{m}$ wide. X-ray CT measurements did show an order of magnitude reduction in porosity (Table 5). If this mechanism is operating, it is expected to not be widely observed throughout the HIP1020RQSA grain structure as the as-built condition contained a very low amount of porosity by volume (0.014%). Also, it was possible to retain such features, due to the rapid quenching rate completed after the HIP/solution hold. Another possible mechanism could be based on the idea that recrystallization begins at melt pool centerlines, where the dislocation density is greatest in some cases (Aota et al., 2021). Along the lines of porosity reduction in general, the standard recommended HIP treatment (AMS, 2774, 2020) used in the baseline condition (100 MPa of argon at 1150°C for 4 h) was certainly sufficient in reducing the as-built pore content from 0.014% to

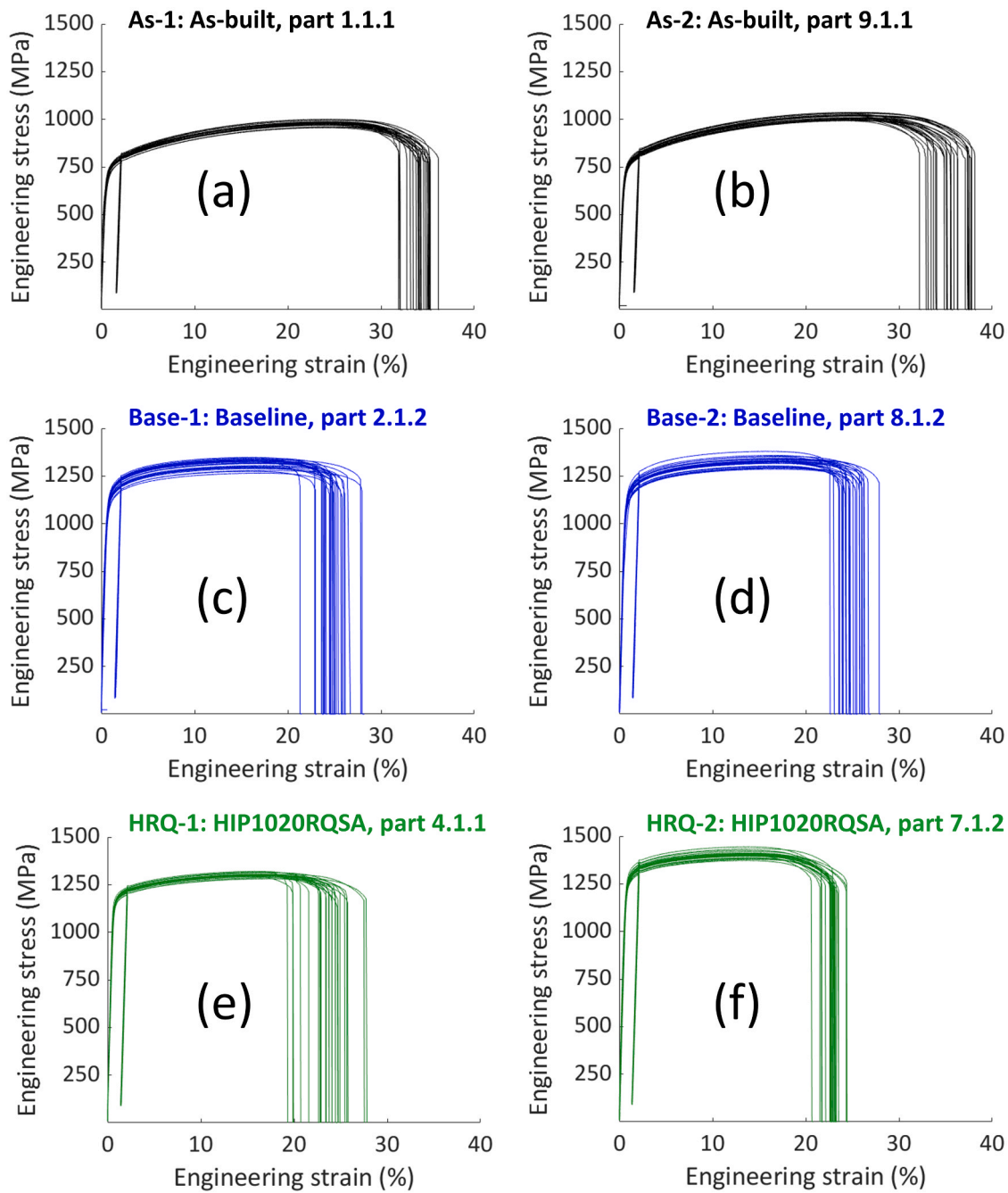


Fig. 11. Engineering stress-strain curves measured in each tensile rack for the (a-b) as-built, (c-d) baseline, and (e-f) HIP1020RQSA material conditions. Note that samples were intentionally unloaded and reloaded at 2% strain to facilitate more accurate elastic modulus measurements.

Table 7

Hardness values measured using the Rockwell C scale. Ranges indicate 1σ standard deviations. All differences are considered extremely significant ($p < 0.001$).

Material condition	Hardness (HRC)
As-built	28.8 ± 0.5
Baseline	43.4 ± 0.4
HIP1020RQ+SA	44.4 ± 0.6

0.0002%. More interestingly, the higher pressure, lower temperature, and shorter time used in the HIP 1020RQSA condition (200 MPa of argon at 1020 °C for 0.5 h) was still sufficient in reducing the porosity more than an order of magnitude from 0.014% to 0.0006%. Overall, the

creation of small equiaxed grains and reduction in porosity should have provided positive contributions to strength and ductility for the HIP1020RQSA condition.

As is the case in many studies, the Laves phase has been characterized and confirmed through various methods such as neutron diffraction (Ferreri et al., 2020), selected area electron diffraction in TEM (Deter et al., 2018), plus morphological and chemical identification by energy dispersive spectroscopy mapping in TEM (Tajyar et al., 2022) and SEM (Watring et al., 2020). In addition, it is common practice to perform FFT analysis of atomic resolution TEM images and STEM-EDS to identify ultrafine γ'' precipitates (Gallmeyer et al., 2020). In this work, STEM-EDS maps, HAADF imaging, and FFT analysis were used to identify phases of interest. A unique finding in the HIP1020RQSA condition was the incomplete dissolution of Laves phase. In a previous

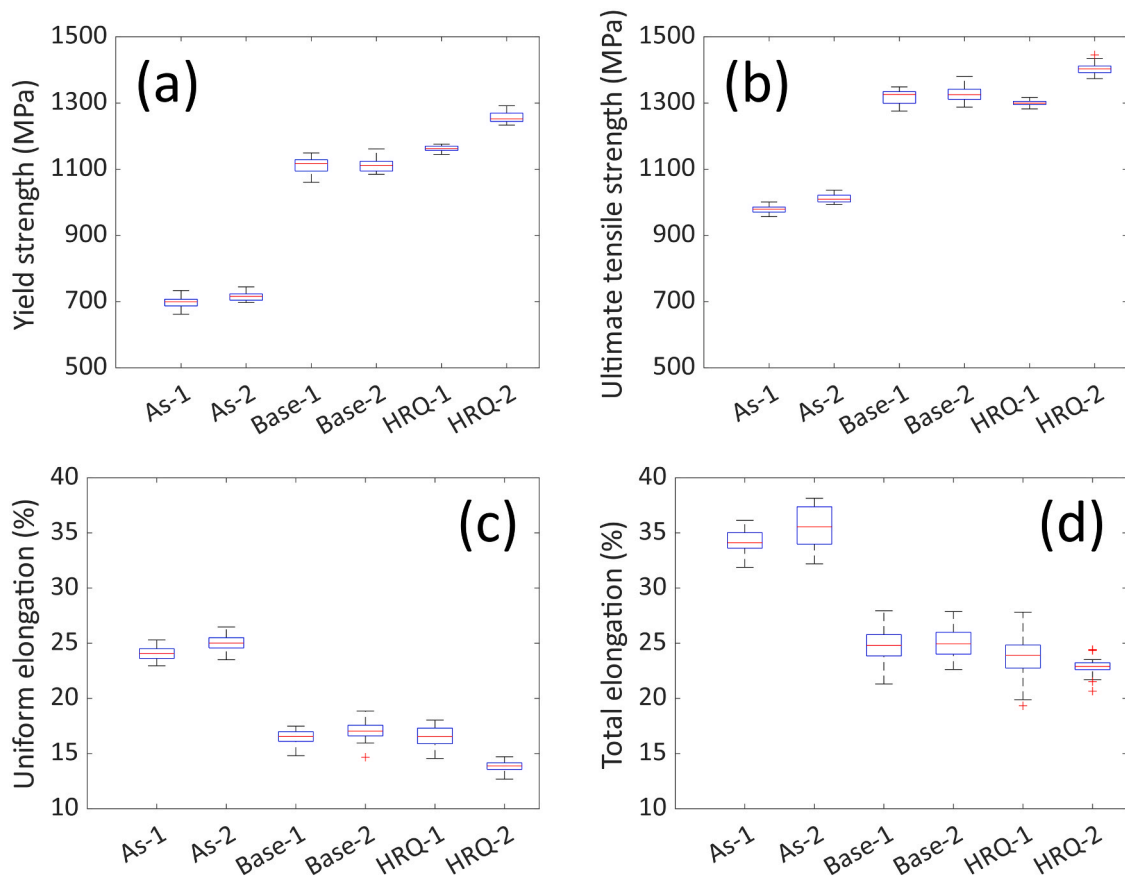


Fig. 12. Engineering tensile properties of (a) 0.2% offset yield strength, (b) ultimate tensile strength, (c) uniform elongation, and (d) total elongation provided for each material condition and tensile rack. In each blue box, the red horizontal line indicates the median. The bottom and top edges of the blue box respectively indicate the 25th and 75th percentiles. Black whiskers extend to the most extreme data points not considered outliers, while the outliers are plotted individually using a red + symbol. An outlier is defined as a value that exceeds three scaled median absolute deviations from the median.

Table 8

Averages of all engineering stress-strain properties. Ranges indicate 1σ standard deviations. All differences are considered extremely significant ($p < 0.001$).

Material condition	Unloading modulus (GPa)	Yield strength (MPa)	Ultimate tensile strength (MPa)	Uniform elongation (%)	Total elongation (%)
As-built	141 ± 5.9	707 ± 17.8	996 ± 20.6	24.5 ± 0.8	34.8 ± 1.6
Baseline	171 ± 7.1	1112 ± 22.4	1321 ± 23.1	16.8 ± 0.8	24.9 ± 1.4
HIP1020RQ+SA	162 ± 3.6	1209 ± 48.0	1351 ± 53.4	15.2 ± 1.5	23.2 ± 1.7

study, a vacuum furnace treatment conducted at 1020 °C for only 0.25 h provided sufficient thermal energy to completely dissolve the Laves phase, whereas the current work (pressurized HIP treatment conducted at 1020 °C and held for a longer time of 0.5 h) did not fully dissolve the Laves phase. It is possible that the isostatic pressure inhibited dissolution through modification of individual diffusion coefficients (Tan et al., 2018) or that nearby Nb-rich carbides remained in too much competition during the shortened solution treatment (Zhao et al., 2020). Within the context that the remaining Laves dispersoids are a consequence of incomplete dissolution, these phases may act as barriers, resulting in a unique combination of Hall-Petch and dispersion strengthening. Nevertheless, the Laves phase is typically described as a brittle phase that is detrimental to ductility (Schirra et al., 2012). While the HIP1020RQSA condition does have the lowest total elongation (23.2%), this is only a minor reduction in comparison to the industry standard baseline condition which had a TE of 24.9% engineering strain. The lack of observed δ phase in the HIP1020RQSA condition, likely due to the rapid quenching rate from the HIP/solution temperature, further supports the notion that only a small amount of ductility was lost due to Laves. The elongated grains parallel to the tensile direction also

contributed positively to the ductility of the HIP1020RQSA condition. As the Laves phase is still present in the HIP1020RQSA condition, inherently any aging conducted will result in under aging from a general perspective as the Laves needs to dissolve into the γ -matrix to fully facilitate precipitation of the intermetallic strengthening phases (γ' and γ''). That said, evidence of both strengthening phases were observed in both the baseline and HIP1020RQSA conditions, although γ' was less defined in the HIP1020RQSA condition and could be due to the rapid quenching conducted after the shortened aging treatment (Babu et al., 2001). While the dislocation density of entangled networks was significantly decreased for the HIP1020RQSA condition, the complete annihilation of the dislocations in the baseline condition were also contributing factors in the HIP1020RQSA condition exhibiting a statistically greater yield and ultimate tensile strength. The high work hardening rate and exceptional ductility of the as-built condition is likely due to a lack of nano-scale strengthening precipitates and minimal porosity. Finally, this work showed that the baseline and HIP1020RQSA conditions exhibited nearly identical work hardening rates, but the latter condition was achieved in approximately one third the total post-processing time.

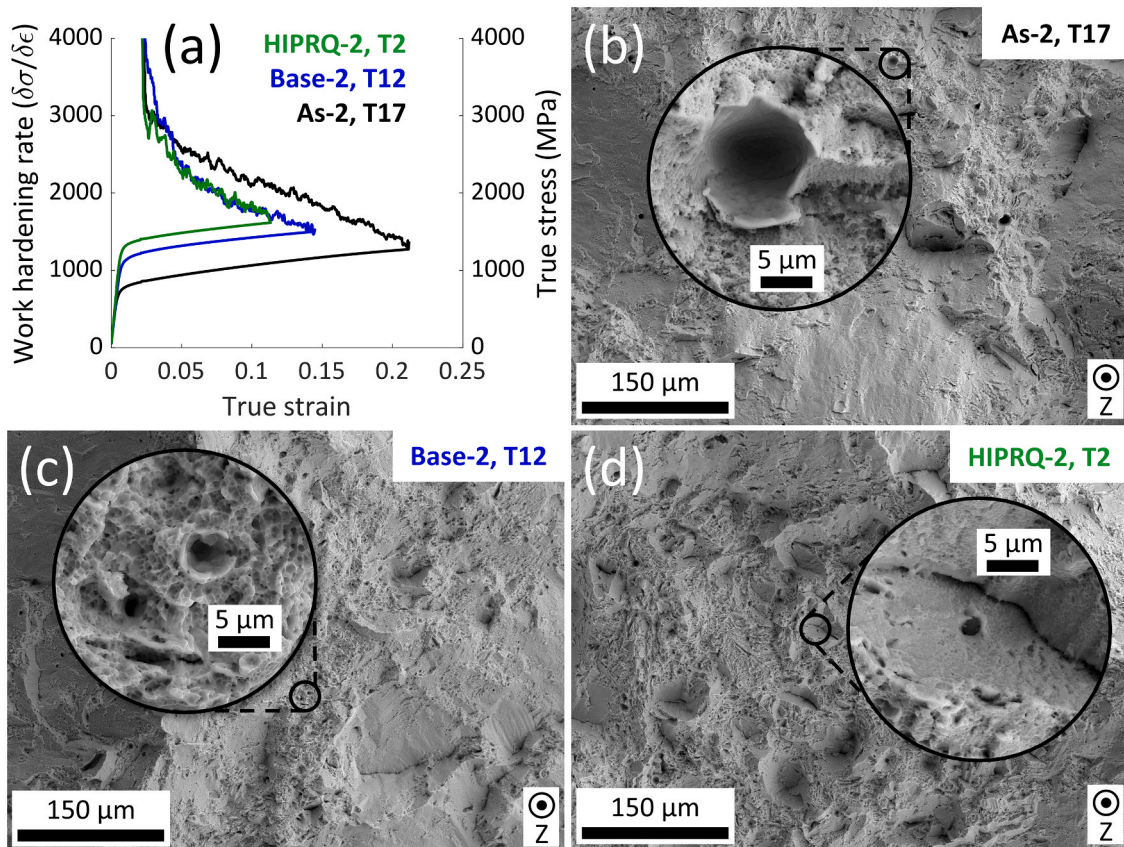


Fig. 13. (a) Representative true stress-strain curves and work hardening rates for each material condition. Note that work hardening rates (left axis) are the jagged curves on top while stress-strain curves (right axis) are the smooth curves on bottom. The corresponding fracture surface of the specimen plotted in (a) was investigated. Secondary electron images were recorded to identify features of interest for the (b) as-built, (c) baseline, and (d) HIP1020RQSA conditions. All fracture surfaces contained microvoid coalescence, the as-built condition revealed plenty of small pores on fracture surfaces, whereas the baseline condition and HIP1020RQSA condition may or may not contain compressed pores on the fracture surfaces.

One future direction for this work could include a peak aging study conducted after the 0.5 h, 1020 °C HIP treatment to optimize the time and temperature necessary for optimized precipitation hardening via single-step aging. Additionally, residual stress measurements on macro- and micro-length scales would further elucidate the contributions of precipitate phases and dislocation networks in the as-built and HIP1020RQSA microstructures. Then, follow on work might investigate the high-temperature mechanical behavior (e.g., tension, creep, and fatigue) of the newly optimized HIP1020RQSA condition and deformation sub-structures would be analyzed to understand dislocation cell impedance during high temperature plastic deformation, cell generation during each stage of creep, and possible cell-driven resistance to fatigue crack initiation and propagation. In addition, the properties along multiple planes of a given part should be conducted to take advantage of the crystallographically oriented grain structures.

5. Summary and conclusions

The goal of this study was to reduce the total post-processing time applied to Inconel 718 parts manufactured by laser powder-bed fusion, while maintaining or improving mechanical performance through microstructure optimization. The complex microstructure in Ni-based super alloys, coupled with rapid solidification and re-melted layers creates a highly ductile grain structure along the build direction, yet with a lack of fully optimized sub-grain structures and strengthening precipitates. Certain applications demand optimized performance along the build direction, balanced with economic advantages of reductions in post-processing time. The tailored heat treatment shown in the present

study in effect removed the conventional stress-relief step, reduced the number of aging steps/times, minimized grain growth, sealed porosity with a minimized hot isostatic pressing soak time, and avoided complete recrystallization. The material structures and properties were characterized with a range of advanced techniques and treated with statistical methods to determine differences. The as-built grain structure contains grains elongated along the build direction and a columnar sub-grain structure comprised of Laves formed along interdendritic boundaries, plus nano-scale carbides, and a high density of clustered dislocation networks. These characteristics, coupled with a relatively low amount of porosity, resulted in the highest work hardening rate of all material conditions. The baseline microstructure, heat treated according to AMS 2774, contains large equiaxed grains with annealing twins, Nb-rich carbides, and nano-scale γ' and γ'' . The nano-scale features sufficiently increased the tensile strength. With respect to the HIP1020RQSA condition, the following conclusions are drawn from this work:

- While the HIP1020RQSA microstructure still contains grains elongated along the build direction, small circular regions of recrystallized grains only a few micrometers in diameter were generated during the high pressure, low temperature/short soak time, and rapidly quenched HIP cycle. In addition, sub-micrometer columnar sub-grain structure with a less defined dislocation network as compared to the as-built condition were present, resulting in a multi-scale grain structure.
- A significant reduction in porosity occurred, even with a shortened HIP time, due to sufficiently high isostatic pressure. Rapid quenching after HIP soak time ensured suppression of δ phase formation.

- Laves phase was still observed along some of the former interdendritic (sub-grain) boundaries in many, but not all cases. Even with incomplete Laves phase dissolution, nano-scale γ' and γ'' was observed after the single aging step that also used rapid quenching.
- Overall, this HIP1020RQSA condition produced the highest hardness and strength, statistically greater than the baseline condition, which was achieved in a third of the total post-processing time.

CRedit authorship contribution statement

Jake T. Benzing: Conceptualization, Investigation, Formal Analysis, Data Curation, Visualization, Project Administration, Writing – Original Draft, Writing – Review & Editing. Nicholas Derimow: Formal Analysis, Writing – Original Draft, Writing – Review & Editing. Orion L. Kafka: Conceptualization, Software, Writing – Review & Editing. Nik Hrabe: Conceptualization, Funding acquisition, Writing – Review & Editing. Philipp Schumacher: Conceptualization, Resources. Donald Godfrey: Conceptualization, Funding acquisition. Chad Beamer: Conceptualization, Investigation, Writing – Review & Editing. Priya Pathare: Investigation, Data Curation. Jay D. Carroll: Resources, Formal Analysis, Writing – Review & Editing. Ping Lu: Investigation, Data Curation. Isaiah Trujillo: Investigation, Formal Analysis. Frank W. DelRio: Conceptualization, Funding acquisition, Writing – Review & Editing.

Declaration of Competing Interest

The authors declare that they have no known competing financial interests or personal relationships that could have appeared to influence the work reported in this paper.

Data availability

Data will be made available on request.

Acknowledgements

Christopher N. James at Metalex Thermal Specialties in Berthoud, CO is acknowledged for performing the vacuum furnace heat treatments in this work (stress relief, solution, two-step age and single-step age). F. W.D was supported by the Center for Integrated Nanotechnologies, a Department of Energy office of Basic Energy Sciences user facility. Sandia National Laboratories is a multimission laboratory managed and operated by National Technology & Engineering Solutions of Sandia, LLC, a wholly owned subsidiary of Honeywell International Inc., for the U.S. Department of Energy's National Nuclear Security Administration under contract DE-NA0003525. This paper describes objective technical results and analysis. Any subjective views or opinions that might be expressed in the paper do not necessarily represent the views of the U.S. Department of Energy or the United States Government.

References

- Aghajani, A., Tewes, J., Parsa, A.B., Hoffmann, T., Kostka, A., Kloewer, J., 2016. Identification of Mo-Rich M₂₃C₆ carbides in alloy 718. *Metall. Mater. Trans. A Phys. Metall. Mater. Sci.* 47, 4382–4392. <https://doi.org/10.1007/s11661-016-3593-5>.
- Akca, E., Gürsel, A., 2015. A review on superalloys and IN718 nickel-based INCONEL superalloy. *Period. Eng. Nat. Sci.* 3 <https://doi.org/10.21533/pen.v3i1.43>.
- AMS2774, 2020. Heat treatment nickel alloy and cobalt alloy parts. SAE Int.
- ANTONSSON, T., Fredriksson, H., 1992. The effect of cooling rate on the solidification of INCONEL 718. *Metall. Trans. A* 23, 3369–3376.
- Aota, L.S., Bajaj, P., Zilnyk, K.D., Jäggle, E.A., Ponge, D., Sandim, H.R.Z., Raabe, D., 2021. Recrystallization kinetics, mechanisms, and topology in alloys processed by laser powder-bed fusion: AISI 316L stainless steel as example. *Materialia* 20, 101236. <https://doi.org/10.1016/j.mtla.2021.101236>.
- ASTM B822, 2020. Standard Test Method for Particle Size Distribution of Refractory Metal Powders and Related Compounds by Light Scattering. ASTM International. <https://doi.org/10.1520/B0822-20.2>.
- ASTM F3055, 2021. Standard Specification for Additive Manufacturing Nickel Alloy (UNS N07718) with Powder Bed Fusion. ASTM International. <https://doi.org/10.1520/F3055-14AR21.Copyright>.

- Babu, S.S., Miller, M.K., Vitek, J.M., David, S.A., 2001. Characterization of the microstructure evolution in a nickel base superalloy during continuous cooling conditions. *Acta Mater.* 49, 4149–4160. [https://doi.org/10.1016/S1359-6454\(01\)00314-7](https://doi.org/10.1016/S1359-6454(01)00314-7).
- Baek, G.Y., Shin, G.Y., Lee, K.Y., Shim, D.S., 2020. Effect of post-heat treatment on the AISI M4 layer deposited by directed energy deposition. *Met. (Basel)* 10. <https://doi.org/10.3390/met10060703>.
- Benzing, J., Hrabe, N., Quinn, T., White, R., Rentz, R., Ahlfors, M., 2019. Hot isostatic pressing (HIP) to achieve isotropic microstructure and retain as-built strength in an additive manufacturing titanium alloy. *Mater. Lett.* 257, 126690 <https://doi.org/10.1016/j.matlet.2019.126690>.
- Cozar, R., Pineau, A., 1973. Morphology of gamma prime and gamma double prime precipitates and thermal stability of Inconel 718 type alloys. *Metall. Mater. Trans. B* 4, 47–59.
- Dehmas, M., Lacaze, J., Niang, A., Viguier, B., 2011. TEM study of high-temperature precipitation of delta phase in inconel 718 alloy. *Adv. Mater. Sci. Eng.* 2011 <https://doi.org/10.1155/2011/940634>.
- Detor, A.J., DiDomizio, R., Sharghi-Moshtaghin, R., Zhou, N., Shi, R., Wang, Y., McAllister, D.P., Mills, M.J., 2018. Enabling large superalloy parts using compact coprecipitation of γ' and γ'' . *Metall. Mater. Trans. A Phys. Metall. Mater. Sci.* 49, 708–717. <https://doi.org/10.1007/s11661-017-4356-7>.
- Ezugwu, E.O., Wang, Z.M., Machado, A.R., 1998. The machinability of nickel-based alloys: a review. *J. Mater. Process. Technol.* 86, 1–16. [https://doi.org/10.1016/S0924-0136\(98\)00314-8](https://doi.org/10.1016/S0924-0136(98)00314-8).
- Fayed, E.M., Shahriari, D., Saadati, M., Brailovski, V., Jahazi, M., Medraj, M., 2020. Influence of homogenization and solution treatments time on the microstructure and hardness of Inconel 718 fabricated by laser powder bed fusion process. *Mater. (Basel)* 13. <https://doi.org/10.3390/ma13112574>.
- Ferreri, N.C., Vogel, S.C., Knezevic, M., 2020. Determining volume fractions of γ , γ' , γ'' , δ , and MC-carbide phases in Inconel 718 as a function of its processing history using an advanced neutron diffraction procedure. *Mater. Sci. Eng. A* 781, 139228. <https://doi.org/10.1016/j.msea.2020.139228>.
- Formenti, A., Eliasson, A., Mitchell, A., Fredriksson, H., 2005. Solidification sequence and carbide precipitation in Ni-base superalloys IN718, IN625 and IN939. *High Temp. Mater. Process.* 24, 239–258. <https://doi.org/10.1515/HTMP.2005.24.4.239>.
- Frazier, W.E., 2014. Metal additive manufacturing: a review. *J. Mater. Eng. Perform.* 23, 1917–1928. <https://doi.org/10.1007/s11665-014-0958-z>.
- Gallmeyer, T.G., Moorthy, S., Kappes, B.B., Mills, M.J., Amin-Ahmadi, B., Stebner, A.P., 2020. Knowledge of process-structure-property relationships to engineer better heat treatments for laser powder bed fusion additive manufactured Inconel 718. *Addit. Manuf.* 31, 100977 <https://doi.org/10.1016/j.addma.2019.100977>.
- Ghosh, S., Ma, L., Ofori-Opoku, N., Guyer, J.E., 2017. On the primary spacing and microsegregation of cellular dendrites in laser deposited Ni-Nb alloys. *Model. Simul. Mater. Sci. Eng.* 25 <https://doi.org/10.1088/1361-651X/aa7369>.
- Haase, C., Kühbach, M., Barrales-Mora, L.A., Wong, S.L., Roters, F., Molodov, D.A., Gottstein, G., 2015. Recrystallization behavior of a high-manganese steel: experiments and simulations. *Acta Mater.* 100, 155–168. <https://doi.org/10.1016/j.actamat.2015.08.057>.
- He, J., Han, G., Fukuyama, S., Yokogawa, K., 1998. Interfaces in a modified Inconel 718 with compact precipitates. *Acta Mater.* 46, 215–223. [https://doi.org/10.1016/S1359-6454\(97\)00221-8](https://doi.org/10.1016/S1359-6454(97)00221-8).
- Heckman, N.M., Ivanoff, T.A., Roach, A.M., Jared, B.H., Tung, D.J., Brown-Shaklee, H.J., Huber, T., Saiz, D.J., Koepke, J.R., Rodelas, J.M., Madison, J.D., Salzbrenner, B.C., Swiler, L.P., Jones, R.E., Boyce, B.L., 2020. Automated high-throughput tensile testing reveals stochastic process parameter sensitivity. *Mater. Sci. Eng. A* 772, 138632. <https://doi.org/10.1016/j.msea.2019.138632>.
- Jena, A.K., Chaturvedi, M.C., 1984. The role of alloying elements in the design of nickel-base superalloys. *J. Mater. Sci.* 19, 3121–3139. <https://doi.org/10.1007/BF00549796>.
- Jiang, R., Mostafaei, A., Pauza, J., Kantzos, C., Rollett, A.D., 2019. Varied heat treatments and properties of laser powder bed printed Inconel 718. *Mater. Sci. Eng. A* 755, 170–180. <https://doi.org/10.1016/j.msea.2019.03.103>.
- Karayagiz, K., Johnson, L., Seede, R., Attari, V., Zhang, B., Huang, X., Ghosh, S., Duong, T., Karaman, L., Elwany, A., Arróyave, R., 2020. Finite interface dissipation phase field modeling of Ni–Nb under additive manufacturing conditions. *Acta Mater.* 185, 320–339. <https://doi.org/10.1016/j.actamat.2019.11.057>.
- Khairallah, S.A., Anderson, A.T., Rubenchik, A., King, W.E., 2016. Laser powder-bed fusion additive manufacturing: physics of complex melt flow and formation mechanisms of pores, spatter, and denudation zones. *Acta Mater.* 108, 36–45. <https://doi.org/10.1016/j.actamat.2016.02.014>.
- Knorovsky, G.A., Cieslak, M.J., Headley, T.J., Romig, A.D., Hammett, W.F., 1989. INCONEL 718: a solidification diagram. *Metall. Trans. A* 20, 2149–2158. <https://doi.org/10.1007/BF02650300>.
- Kou, S., 2003. *Welding metallurgy*, 2nd ed. Wiley-Interscience, Hoboken, NJ.
- Krueger, H., 2017. Standardization for additive manufacturing in aerospace. *Engineering* 3, 585. <https://doi.org/10.1016/j.eng.2017.05.010>.
- Kruth, J.P., Leu, M.C., Nakagawa, T., 1998. Progress in additive manufacturing and rapid prototyping. *CIRP Ann. - Manuf. Technol.* 47, 525–540. [https://doi.org/10.1016/S0007-8506\(07\)63240-5](https://doi.org/10.1016/S0007-8506(07)63240-5).
- Kuo, Y.L., Nagahari, T., Kakehi, K., 2018. The effect of post-processes on the microstructure and creep properties of Alloy718 built up by selective laser melting. *Mater. (Basel)* 11. <https://doi.org/10.3390/ma11060996>.
- Lambarri, J., Leunda, J., García Navas, V., Soriano, C., Sanz, C., 2013. Microstructural and tensile characterization of Inconel 718 laser coatings for aeronautic components. *Opt. Lasers Eng.* 51, 813–821. <https://doi.org/10.1016/j.optlaseng.2013.01.011>.

- Li, X., Shi, J.J., Cao, G.H., Russell, A.M., Zhou, Z.J., Li, C.P., Chen, G.F., 2019. Improved plasticity of Inconel 718 superalloy fabricated by selective laser melting through a novel heat treatment process. *Mater. Des.* 180 <https://doi.org/10.1016/j.matdes.2019.107915>.
- Liu, L., Ding, Q., Zhong, Y., Zou, J., Wu, J., Chiu, Y.L., Li, J., Zhang, Z., Yu, Q., Shen, Z., 2018. Dislocation network in additive manufactured steel breaks strength–ductility trade-off. *Mater. Today* 21, 354–361. <https://doi.org/10.1016/j.mattod.2017.11.004>.
- Mahadevan, S., Nalawade, S., Singh, J.B., Verma, A., Paul, B., Ramaswamy, K., 2010. Evolution of δ phase microstructure in alloy 718. 7th Int. Symp. Superalloy 718 Deriv. 2010 2, 737–750. <https://doi.org/10.1002/9781118495223.ch57>.
- Mecking, H., Kocks, U.F., 1981. Kinetics of flow and strain hardening. *Acta Met* 29, 1865–1875. [https://doi.org/10.1016/0001-6160\(81\)90112-7](https://doi.org/10.1016/0001-6160(81)90112-7).
- Moser, N.H., Landauer, A.K., Kafka, O.L., 2023. Impy3d: Image processing in python for 3D image stacks. *Natl. Inst. Stand. Technol. Public Data Repos.* <https://doi.org/10.18434/mds2-2806>.
- Pröbstle, M., Neumeier, S., Hopfenmüller, J., Freund, L.P., Niendorf, T., Schwarze, D., Göken, M., 2016. Superior creep strength of a nickel-based superalloy produced by selective laser melting. *Mater. Sci. Eng. A* 674, 299–307. <https://doi.org/10.1016/j.msea.2016.07.061>.
- Radavich, J.F., 2012. The Physical Metallurgy of Cast and Wrought Alloy 718 229–240. https://doi.org/10.7449/1989/superalloys_1989_229_240.
- Schirra, J.J., Caless, R.H., Hatala, R.W., 2012. The Effect of Laves Phase on the Mechanical Properties of Wrought and Cast + HIP Inconel 718 375–388. https://doi.org/10.7449/1991/superalloys_1991_375_388.
- Slama, C., Servant, C., Cizeron, G., 1997. Aging of the Inconel 718 alloy between 500 and 750C. *J. Mater. Res.* 12, 2298–2316.
- Sundararaman, M., Mukhopadhyay, P., Banerjee, S., 1992. Some aspects of the precipitation of metastable intermetallic phases in INCONEL 718. *Metall. Trans. A* 23, 2015–2028. <https://doi.org/10.1007/BF02647549>.
- Tajyar, A., Brooks, N., Holtham, N., Rowe, R., Newell, D.J., Palazotto, A.N., Davami, K., 2022. Effects of a modified heat-treatment on microstructure and mechanical properties of additively manufactured Inconel 718. *Mater. Sci. Eng. A* 838, 142770. <https://doi.org/10.1016/j.msea.2022.142770>.
- Tan, L., He, G., Liu, F., Li, Y., Jiang, L., 2018. Effects of temperature and pressure of hot isostatic pressing on the grain structure of powder metallurgy superalloy. *Mater. (Basel)* 11. <https://doi.org/10.3390/ma11020328>.
- Tao, P., Li, H., Huang, B., Hu, Q., Gong, S., Xu, Q., 2019. The crystal growth, intercellular spacing and microsegregation of selective laser melted Inconel 718 superalloy. *Vacuum* 159, 382–390. <https://doi.org/10.1016/j.vacuum.2018.10.074>.
- Tillmann, W., Schaak, C., Nellesen, J., Schaper, M., Aydinöz, M.E., Hoyer, K.P., 2017. Hot isostatic pressing of IN718 components manufactured by selective laser melting. *Addit. Manuf.* 13, 93–102. <https://doi.org/10.1016/j.addma.2016.11.006>.
- Varela, J., Merino, J., Pickett, C., Abu-Issa, A., Arrieta, E., Murr, L.E., Wicker, R.B., Ahlfors, M., Godfrey, D., Medina, F., 2020. Performance characterization of laser powder bed fusion fabricated inconel 718 treated with experimental hot isostatic processing cycles. *J. Manuf. Mater. Process.* 4 <https://doi.org/10.3390/JMMP4030073>.
- Watring, D.S., Benzing, J.T., Hrabec, N., Spear, A.D., 2020. Effects of laser-energy density and build orientation on the structure–property relationships in as-built Inconel 718 manufactured by laser powder bed fusion. *Addit. Manuf.* 36, 101425 <https://doi.org/10.1016/j.addma.2020.101425>.
- Zhang, S., Liu, Z., Wang, B., Ren, X., Khan, A.M., Zhao, M., 2021. Phase transition and dynamic recrystallization mechanisms of white layer formation during turning superalloy Inconel 718. *J. Mater. Res. Technol.* 15, 5288–5296. <https://doi.org/10.1016/j.jmrt.2021.11.004>.
- Zhao, Y., Li, K., Gargani, M., Xiong, W., 2020. A comparative analysis of Inconel 718 made by additive manufacturing and suction casting: microstructure evolution in homogenization. *Addit. Manuf.* 36, 101404 <https://doi.org/10.1016/j.addma.2020.101404>.
- Zhu, Z.G., Nguyen, Q.B., Ng, F.L., An, X.H., Liao, X.Z., Liaw, P.K., Nai, S.M.L., Wei, J., 2018. Hierarchical microstructure and strengthening mechanisms of a CoCrFeNiMn high entropy alloy additively manufactured by selective laser melting. *Scr. Mater.* 154, 20–24. <https://doi.org/10.1016/j.scriptamat.2018.05.015>.